REPORT DOCUMENTATION PAGE

AFRL-SR-BL-TR-02-

6024

1. AGENCY USE ONLY *(Leave blank)*	2. REPORT DATE	3. REPORT TYPE AND DATES COVERED
		01 Jul 96 to 30 Jun 99 FINAL

4. TITLE AND SUBTITLE
(AASERT 96) Solid State Microwave and Millimeter Electronics

5. FUNDING NUMBERS
61103D
3484/TS

6. AUTHOR(S)
Professor Wang

7. PERFORMING ORGANIZATION NAME(S) AND ADDRESS(ES)
Univeristy of California
405 Hilgard Avenue
Los Angeles, CA 90024-1406

8. PERFORMING ORGANIZATION REPORT NUMBER

9. SPONSORING/MONITORING AGENCY NAME(S) AND ADDRESS(ES)
AFOSR/NE
801 North Randolph Street Rm 732
Arlington, VA 22203-1977

10. SPONSORING/MONITORING AGENCY REPORT NUMBER

F49620-96-1-0302

11. SUPPLEMENTARY NOTES

12a. DISTRIBUTION AVAILABILITY STATEMENT
APPROVAL FOR PUBLIC RELEASED; DISTRIBUTION UNLIMITED

12b. DISTRIBUTION CODE

AIR FORCE OFFICE OF SCIENTIFIC RESEARCH (AFOSR)
NOTICE OF TRANSMITTAL DTIC. THIS TECHNICAL REPORT
HAS BEEN REVIEWED AND IS APPROVED FOR PUBLIC RELEASE
LAW AFR 190-12. DISTRIBUTION IS UNLIMITED.

13. ABSTRACT *(Maximum 200 words)*

There has been a great deal of interest in recent years in the investigation
of signals in the terahertz frequency range of the electromagnetic spectrum.
One impediment to this ongoing research is the lack of useful sources of
energy and detectors in this spectral region. One promising solution to this
problem is the use of non-linear optics and the process of difference
frequency generation (DFG). This dissertation investigates the use of DFG in
dielectric waveguide structures ultilizing the resonant enhancement of
asymmetric quantum wells.

20020130 263

14. SUBJECT TERMS			15. NUMBER OF PAGES
			16. PRICE CODE

17. SECURITY CLASSIFICATION OF REPORT	18. SECURITY CLASSIFICATION OF THIS PAGE	19. SECURITY CLASSIFICATION OF ABSTRACT	20. LIMITATION OF ABSTRACT
UNCLASSIFIED	UNCLASSIFIED	UNCLASSIFIED	UL

FINAL TECHNICAL REPORT

SOLID STATE AND MICROWAVE AND MILLIMETER ELECTRONICS

AASERT

W,H

AWARD NUMBER F49620-96-1-0302

PRINCIPAL INVESTIGATOR:
PROFESSOR
KANG L. WANG

UNIVERSITY OF CALIFORNIA AT
LOS ANGELES

The projects carried out are: (1) Microwave properties of series-connected resonant tunneling diodes (RTDs), (2) Transport properties and energy band analysis in a RTD, and (3) Difference frequency generation (DFG) in a quantum well waveguide structure. Research continued into the transport properties of RTDs with emphasis focused on explaining why current peaks are observed when the energy bands of the quantum wells are aligned with the emitter energy levels rather than with the connected wells as expected. In addition, structures were designed to have series connected RTDs operate in the negative differential resistance (NDR) region simultaneously. In this way, the output microwave power could be enhanced dramatically. Ideally, this would occur by controlling the bias voltage on each RTD separately, but given the thick nesses of the layers involved, this is not yet possible with today's technology. By optimizing the spacer layers and drift regions between the RTDs, however, improvements in simultaneous operation were achieved. S-parameter characterization of the RTDs also continued with maximum operating frequencies of greater than 16 GHz achieved with the InGaAs/AlAs structure. In addition RTDs using GaN material, which were provided by an outside manufacturer, were investigated, and attempts to obtain NDR data were made. It was found that the material quality of these devices was not good enough to support NDR operation. Attempts are currently underway to improve the material properties and achieve NDR in these devices. DFG research in the IR region was concluded and the current emphasis is on producing long wavelength signals. A bolometer has been contracted in order to detect the long wavelength signals, which are expected to be generated. Theoretical studies of the propagation of optical and millimeter waves through various types of semiconductor waveguide structures has been conducted.

Since two separate lasers of sufficient power at the wavelength of interest are not available, research has been conducted by splitting the output of a single mode locked Ti: sapphire laser into two component parts which are then separately filtered using narrowband filters into two fields with wavelengths which are separated by 10nm. In this manner, an output signal with a wavelength of approximately 81☐m should be generated. The laser is easily tunable over a wide range so the output power can be monitored while varying the input fields around the fundamental absorption edge of GaAs in order to examine the trade-offs between resonance enhancement and losses due to absorption and maximize the output power. The overall goal of this unit remains to create viable energy sources in the millimeter wave region.

The following have been published:

1. J. Jo, K. Alt, and K.L. Wang, "Observation of new type resonances in triple barrier resonant tunneling diodes," J. Appl. Phys. 82 (6), 2980-2983, September 15, 1997.
2. J. Jo, K. Alt, and K.L. Wang, "Effect of doping density on capacitance of resonant tunneling diodes," J. Appl. Phys. 82 (10), 5206-5209, November 15, 1997.
3. J. Jo, Y.I. Choi, D.M. Kim, K. Alt, and K.L. Wang, "Observation of resonances by individual energy levels in InGaAs/AlAs triple barrier resonant tunneling diodes," Japanese Journal of Applied Physics, 37, 18-20, March 1998.

Post Doctoral
        Kevin Wang
        Richard Li
Graduate Students
        Kevin Alt
Technology Transfer
None

Invention
None

Honors and Awards, Advisory Functions
None

Thesis
Ph.D. (see attached).

UNIVERSITY OF CALIFORNIA

Los Angeles

Difference Frequency Generation of Infrared Waves

In Asymmetric Quantum Wells

A dissertation submitted in partial satisfaction of the

requirements for the degree Doctor of Philosophy

in Electrical Engineering

by

Kevin Wade Alt

1999

Table of Contents

VITA

April 14, 1959	Born, Washington, D.C.
1981	B. S., Electrical Engineering U.S. Naval Academy Annapolis, Maryland
1984-1986	Weapons Officer USS Sea Devil (SSN 664) Charleston, South Carolina
1988	M. S., Electrical Engineering University of California, Los Angeles Los Angeles, California
1988-1991	Engineer Officer USS Oklahoma City (SSN 723) Norfolk, Virginia
1992-1994	Board Member Nuclear Propulsion Examining Board Pearl Harbor, Hawaii
1995-1999	Research Assistant Device Research Laboratory University of California, Los Angeles Los Angeles, California

PUBLICATIONS AND PRESENTATIONS

Kevin Alt and Patrick Sullivan, "Investigation of Thick Oxide N-Type Metal Oxide Semiconductors," Presentation at SPAWAR Systems Center, San Diego, Integrated Circuit Fabrication Facility, 28 April 1999.

C. Y. Chen, Tineke Thio, K. L. Wang, K. W. Alt, and P. C. Sharma, "Persistent photoconductivity in Si delta-doped GaAs at low doping concentration," *Applied Physics Letters,* **73**, 3235-3237, 30 November 1998.

ABSTRACT OF THE DISSERTATION

Difference Frequency Generation of Infrared Waves

in Asymmetric Quantum Wells

by

Kevin Wade Alt

Doctor of Philosophy in Electrical Engineering

University of California, Los Angeles, 1999

Professor Kang L. Wang, Chair

There has been a great deal of interest in recent years in the investigation of signals in the terahertz frequency range of the electromagnetic spectrum. One impediment to this ongoing research is the lack of useful sources of energy and detectors in this spectral region. One promising solution to this problem is the use of non-linear optics and the process of difference frequency generation (DFG). This dissertation investigates the use of DFG in dielectric waveguide structures utilizing the resonant enhancement of asymmetric quantum wells.

The $Al_xGa_{(1-x)}As/GaAs$ material system was investigated for this approach. Samples were grown in a molecular beam epitaxy chamber and characterized via photoluminescence and Raman spectroscopy to verify their composition. A series of investigations was conducted in homogenous waveguide structures utilizing a laser diode mixed with a tunable Ti:sapphire solid state laser. Both waveguide and non-linear phase matching were investigated and demonstrated.

Chapter 1

Motivation and Objectives

Recently, there has been a great deal of interest in the investigation of different means of millimeter and infrared wave generation using nonlinear optical waveguide structures coupled with asymmetric quantum wells.[1-3] Semiconductor infrared and millimeter wave sources are essential for a broad spectrum of applications ranging from electronic warfare, radar mapping in the vacuum of deep space, to wireless communication systems. Currently there are few good sources of electro-magnetic radiation in the so-called quasi-optical region from wavelengths of 30 to 300 μm. If a small power source could be devised, then external waveguide and microwave amplifiers could be designed to boost the signal to the desired level.

The material chosen for this research is the GaAs/AlGaAs III-V compound semi-conductor system. This particular choice was made based on a number of factors. First, these materials are direct bandgap semiconductors over much of the compositional range, offering better optical qualities than indirect type materials. Second, the technology for fabrication and growth of samples using these materials is fairly mature and well known. The lattice constants of GaAs and AlGaAs are 5.6533 and 5.6611 Angstroms, respectively, so they are very well suited for epitaxial growth.[4] Structures of virtually any thickness can be grown without fear of exceeding the critical thickness for dislocation free crystals. The growth and characterization of the samples used in this research will be discussed in Chapter 2. Third, the second order non-linear susceptibility

The other motivation for choosing this material is the ability to accurately grow quantum well structures. It has been shown that asymmetric quantum well structures can enhance the already large $\chi^{(2)}$ value of this system with the associated potential of achieving even larger power output levels.[6]

Thus, the objective at the outset is to grow and characterize waveguide structures out of GaAs/Al$_x$Ga$_{(1-x)}$As/AlAs materials and investigate their DFG properties. We would like to characterize the resonance enhancement provided by the quantum well structures and evaluate their suitability for monolithic devices in practical applications.

Chapter 2

Growth and Characterization of Samples

2.1 Introduction

All of the samples used in this research were grown in a Perkin Elmer 430 molecular beam epitaxy (MBE) chamber. A picture of this MBE chamber is shown as Figure 2-1. Of particular interest in the picture are the Reflection High Energy Electron Diffraction (RHEED) screen and associated charge coupled device (CCD) camera evident in the left foreground. Also seen at top dead center is the residual gas analyzer (RGA) RF matching assembly. This equipment was used to measure the relative flux levels between the different atomic species during the growth process as described later. The MBE chamber consists of a sample holder with built-in heater, Knudsen effusion cells for Al, Ga, and Si material, and an As crucible with high temperature cracker to break the sublimated As from As_4 to As_2. It has been found that growth of the samples using As_2 instead of As_4 lengthens the source life and lowers the chamber background pressure since a lower As flux can be used in this case. Growth temperatures were monitored by a backside mounted thermocouple along with an optical pyrometer.

In this chapter we shall describe the growth process and sample characterization procedures which were used during the course of this research. As shown in Chapter 5, material parameters such as the index of refraction, are critical to achieving the proper phase matching relationships required for any kind of power to be developed using the DFG process. All of the pertinent parameters directly depend on the Aluminum (Al)

content of the crystal along with the overall crystal quality. Due to the importance of these topics in the overall research, we shall spend some time discussing them.

2.2 Sample Growth and Preparation

2.2.1 Sample Cleaning

All of the samples were grown on [100] orientated semi-insulating GaAs substrates. The wafers were epitaxial (epi) growth ready when received from the manufacturer, however, these three inch wafers were cleaved into smaller pieces to conserve material. Due to possible contamination of the surface during the cleaving process, an organic cleaning and subsequent etching procedure was developed and followed to ensure that the sample surfaces were atomically clean prior to loading into the MBE chamber. The cleaning procedure consisted of dipping for five minutes each in solutions of chloroform, acetone, and methanol. This cleaning was followed by a five minute soak in de-ionized (DI) water. Following the organic cleansing, the samples were etched for four minutes in a solution of H_2SO_4, H_2O_2, and H_2O at a ratio of 8:1:1. This solution is exothermic, so it was cooled in an ice bath after mixing for approximately 45 minutes to produce an etchant temperature of 15 +/- 2 degrees. The etch rate is dependent upon the etchant temperature, so it was important to maintain a consistent value for repeatable results. This serves to etch approximately 1 μm of material off of the surface and makes it atomically clean in preparation for epitaxial growth. It was also determined through subsequent experience that the thermal cleaning of the samples took less time and produced a better surface reconstruction RHEED pattern than when samples

species show a distinct set of two peaks due to the presence of isotopes naturally occurring at amu 69 and 71 with a 60/40 ratio. During routine growth operations, the so-called *half mass* peaks were monitored since their magnitudes are closer together and are thus more convenient to monitor. They also fall just above the region where we monitor for contaminants, so one can more completely check the entire system by using these peaks. The RGA operates on the principle of a quadrupole mass spectrometer, and atoms which are doubly ionized will appear on the spectrum at the half mass values of the parent atoms. Ga has a much greater tendency to become doubly ionized than As, so when the proper flux ratio is set, the half mass peak ratio was approximately 2:1. Once the optimum flux ratio was determined, the value from the RGA was recorded and used in subsequent growths.

Prior to placing the samples in the growth chamber, they were preheated in an adjacent tube maintained in UHV conditions to outgas the majority of the atmospheric gases picked up when the samples were loaded on the blocks. The samples were outgassed for 30-60 minutes at a temperature of 300 C. During the outgassing process, the tube pressure was monitored to determine when the outgas was complete. Typically the tube pressure would rise from its base value of 5×10^{-10} to 1×10^{-7} Torr during the outgas illustrating the importance of this procedure in minimizing the amount of contaminants introduced into the growth chamber.

After loading in the MBE chamber, the samples were heated to approximately 570 C over 30 minutes. As the sample temperature was increased above 300 C, the As shutter was opened and an As overpressure provided due to the adsorption of As from the

Of critical importance in this research was the accurate determination of layer thicknesses. The layer thickness determines the phase matching condition for the waveguide structure, and as will be shown later in Chapter 5, the phase mismatch is fairly sensitive to the sample thickness. In order to calibrate the growth rate, RHEED oscillations were observed and recorded. It has been shown that the RHEED oscillation period corresponds to the deposition of one mono-layer of material when monitoring the

Figure 2-2. RHEED Oscillations on [100] GaAs
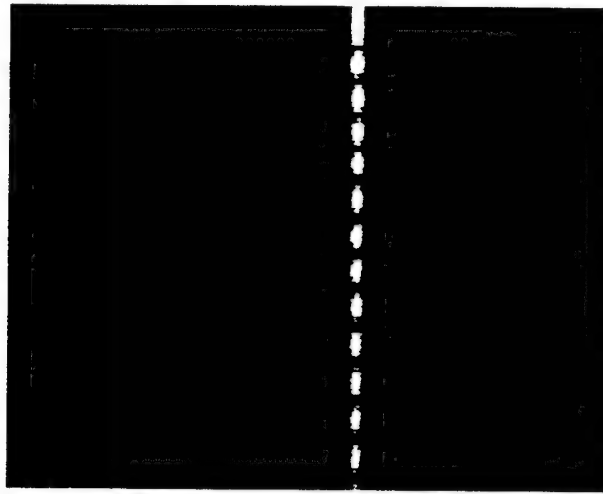
[001] surface, and in this manner, growth rates can be accurately determined.[2] The growth rate is determined by equation 2.1. Figure 2-2 shows the RHEED oscillation

$$R = f_{osc} * 1.01772(\mu m / hr)$$
(2.1)

observed during a calibration run. The image shows a particular pixel on the RHEED screen imaged on the CCD camera and then recorded vs. time. The time period shown is

11

on the order of 15 seconds. It's interesting to note that the growth rate is coincidentally almost nearly identical to the oscillation frequency. The RHEED oscillation patterns are observed at various values of source temperature, resulting in growth rate vs. source temperature curves for each of the Al sources and for the Ga source. Figure 2-3 shows a calibration curve obtained in this manner for the Al2 source. The growth rates obtained in this manner were compared with Alfa Step measurements and agreement between the two methods was within 1 percent. Calibration checks were completed prior to the growth of all waveguide structures to minimize the errors in the as-grown thickness values. To calibrate the Si source, a series of samples were grown with different source temperatures, and then the carrier concentration was determined using standard Hall measurements. The flux rate of the source vs. temperature was then determined based on the doping and the growth rate, and a curve similar to Figure 2-3 was obtained.

2.3 Sample Characterization

2.3.1 Introduction

Of equal importance in the obtaining of proper phase matching is an accurate determination of the Al content of the $Al_xGa_{(1-x)}As$ layers. As will be discussed in Chapter 5, the index of refraction of these materials varies with x, and a change of x from .14 to .16 will change the index of refraction of the waveguide area from 3.483 to 3.470 at 890 nm.[3] This will have a significant impact on the phase matching condition, so it is crucial to accurately determine the Al composition. In the case of our samples, the area of interest was principally in the waveguide region which was typically underneath a

layer of AlAs which formed the upper waveguide boundary and a layer of GaAs which served to protect the AlAs from the atmosphere. As is detailed in the following sections, some of the characterization techniques required the baring of the waveguide region to the surface. As a result, an etchant was utilized which would rapidly etch the AlAs layers while etching the waveguide region which was of low Al concentration at a much slower rate. The etchant used consisted of a mixture of H_3PO_4:H_2O_2:H_2O in a 4:1:20 ratio. It was found that the etch rate for this solution was on the order of 2000 Angstroms/second for AlAs material while only on the order of 60 Angstroms/second for GaAs and low Al content $Al_xGa_{(1-x)}As$ materials. Figure 2-4 shows the data from a test run on a sample consisting of 1.1 μm of AlAs grown over 1.2 μm of waveguide like material composed of $Al_{.14}Ga_{.86}As$, with a 50 Angstrom cap of GaAs. A simple mask was developed in order to prevent etching in a rectangular region, and then etching was conducted at 5 second intervals followed by measurement of the protected region height on the Alfa step profiler. As is clearly evident in Figure 2-4, the solution quickly etched away the AlAs barrier material and then slowed when reaching the waveguide region. Using this technique, pieces of each waveguide structure grown were cut off and then etched to reveal the waveguide region for characterization study. The standard waveguide structure, consisting of 5000 Angstrom barriers, was etched for 45 seconds to ensure that the center of the waveguide region would be reached. Following the removal of the barrier material, the sample was characterized first by Raman spectroscopy to ensure that the proper region had been reached.
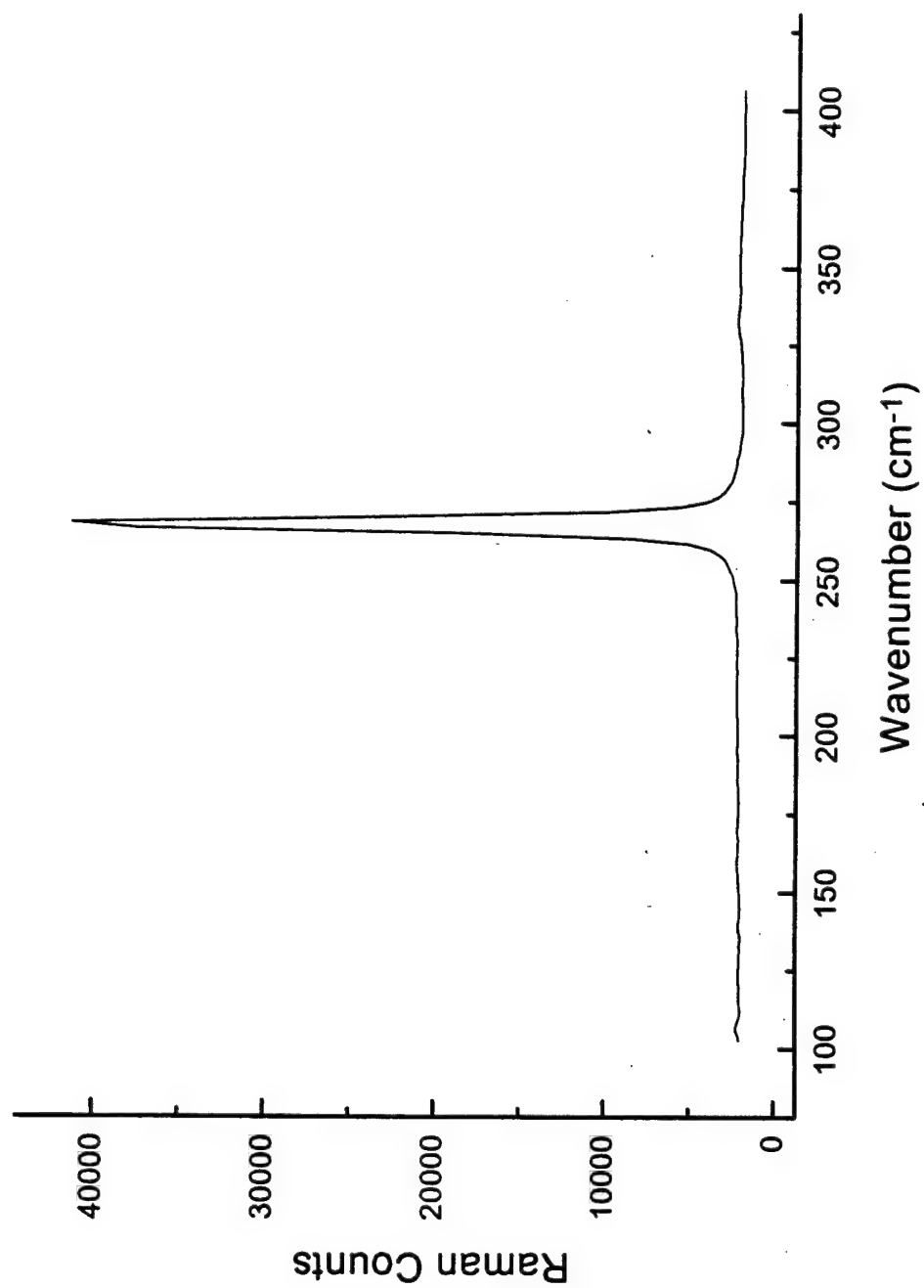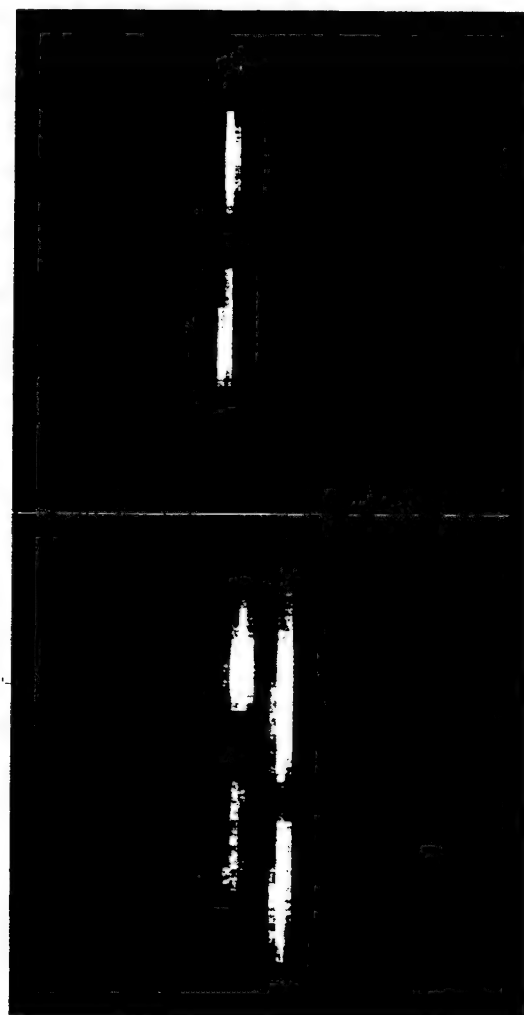
Figure 2-5. Raman Scan of [1,10] GaAs Substrate

GaAs and AlAs, respectively. For this particular phonon, a change in Al content from .10 to .11 shifts the frequency from 366.2 to 366.7 which is well within the measuring capability of our equipment. Hence, the samples were etched down to the waveguide region and then the LO phonon frequency was measured. It was found that the perturbation on the GaAs phonon was more difficult to measure due to interference from the substrate region, so measurements were made based on the perturbation of the AlAs phonons. These results were used to provide a quality assurance check with the photoluminescence (PL) measurements which are described in the following section.

Before the selective etching process was developed, we attempted to utilize Raman spectroscopy on the [110] side faces to determine the Al content, since the waveguide region would be exposed along the sides. And in fact, the waveguide region, AlAs barrier layers and GaAs cap regions are all distinguishable on these Raman side scans, and the transition from the unperturbed GaAs TO phonon from the substrate to the perturbed TO phonon in the waveguide region is easily recognized. Figure 2-5 shows the [110] scan on the substrate area. The GaAs TO phonon is readily identified at 268.1 cm^{-1} and shows the good crystal quality of the region. Figure 2-6 shows the [110] scan of the waveguide region. The perturbed AlAs TO phonon is predominant in the scan at 360.9 cm^{-1}. The GaAs phonon also shows the perturbation of the Al content being shifted down to about 267 cm^{-1}. The data below the GaAs TO phonon is due to the combination of noise and the effects of alloying GaAs and AlAs. In addition, the waveguide region is very close to the top surface of the sample, and there is considerable scattering from the edge roughness nearby. The Raman signal strength is also weaker which makes the

(a)

(b)

Figure 2-8. Raman Spectrographic Images of [110] Waveguide Region
(a) GaAs like phonon (b) AlAs like phonon

21

showing *where* the photons with the selected Stokes shift originated. Figure 2.8 shows side by side images of the above sample. The left hand image had the GaAs like phonon frequencies selected while the right hand image shows the AlAs like frequencies. This method was used to give quantitative data on the uniformity of growth and the quality of the waveguide region. It was also found that the intensity of the AlAs phonons decreased over time after the sample was cleaved. This was due to the formation of oxide on the surface and again was used to determine the overall cleanliness of the waveguide face.

2.3.3 Photoluminescence

PL is a accurate and fairly easy way to determine the overall crystal quality and Al content. PL consists of exciting the sample with a high energy laser source with energy greater than the bandgap energy, generating electron-hole pairs (ehp's).[8] The ehp's recombine by one of several mechanisms. Photons are emitted for radiative recombination, and these are the processes that we are interested in. The most difficult part of the measurement is that for good results, PL should be done at extremely low temperatures, typically at 4.2 K. The mechanisms for radiative recombination are chiefly band to band, free exciton (FX), exciton bound to a donor (DX), and exciton bound to an acceptor (AX). Due to the large electron orbital radii, band to band recombination is not strong at low temperatures, and the excitonic states dominate. At low Al concentrations, the excitonic contributions have distinct peaks, but as the Al content increases, these excitonic peaks are not resolved due to alloy broadening, and a single excitonic peak

emerges for Al concentrations greater than .10.[9] Equation 2.4 relates the energy of the

$$BE(eV) = 1.514 + 1.463 * x \qquad (2.4)$$

bound exciton (BE) peak vs. Al content. This equation is valid for temperatures up to 40 K and for Al concentrations below .38. Figure 2-9 shows the PL spectra at 20 K of a waveguide test sample grown with a design Al concentration of .19. The curve shows the BE peak at 1.766 eV, corresponding to an Al concentration of .172, which is typical accuracy for our chamber (+/- .02). Raman measurements on this sample indicated an Al concentration of .152 as discussed earlier. Also evident in the spectra is a broad impurity like peak at 1.746 eV which has a stronger intensity than the BE peak. This indicates an $Al_xGa_{(1-x)}As$ crystal of moderate quality. The impurity is most likely carbon since our system uses a carbon source for p-type doping, and carbon contamination has been a problem in the past. The binding energy of carbon as a function of Al content is given by equation 2.5.[9] It is seen that at this Al concentration, the binding energy is 28.0 meV,

$$Ea(meV) = 26.7 + 5.75 * x + 123 * x^{3.4} \qquad (2.5)$$

which is higher than the observed difference between the peak and the BE peak. The BE peak has been verified by confirmation of the Al content by other measurements including X-ray diffraction. In addition, This structure was observed on the majority of the samples and is still under investigation. Future plans include growing samples on different blocks without utilizing In bonding to see if contamination from the block is the source of the signal.

Chapter 3

Difference Frequency Generation

3.1 Introduction

Many good texts have been written on the subject of DFG, and we shall not try to reprint them here.[1-2] One of the most authoritative (and best) books remains the landmark book of Bloembergen printed over 30 years ago.[3] We will endeavor, however, to provide enough background material such that this paper may serve as a stand alone document whereby the interested reader will not have to dust off the referenced textbooks in order to follow the subsequent discussions presented.

3.2 First Order or Linear Interactions

Every discussion of electromagnetic (EM) theory traditionally begins with Maxwell's famous equations, and we will not deviate here. Maxwell's equations in MKS

$$\nabla \cdot D = \rho \tag{3.1}$$

$$\nabla \cdot B = 0 \tag{3.2}$$

$$\nabla \times H = J + \frac{\partial D}{\partial t} \tag{3.3}$$

$$\nabla \times E = -\frac{\partial B}{\partial t} \tag{3.4}$$

units and differential form are presented as equations 3.1 through 3.4. These equations are the basis for much of the discussion which follows.

phenomena of absorption, reflection, and refraction. In general, it is a complex quantity given by equation 3.7. The index of refraction, $n(\omega)$, and the dielectric constant, $\varepsilon(\omega)$ are related to the real part of the susceptibility as given by equation 3.8. The absorption coefficient, $\alpha(\omega)$, is related to the imaginary part of the susceptibility by equation 3.9.[4]

$$\chi_{jk}^{(1)} = \chi_{jk}^{'(1)} + j\chi_{jk}^{''(1)} \tag{3.7}$$

$$n_{jk}^2(\omega) = \frac{\varepsilon_{jk}^2(\omega)}{\varepsilon_0} = 1 + \chi_{jk}^{'(1)} \tag{3.8}$$

$$\alpha(\omega) = \left(\frac{\omega}{c}\right)\chi_{jk}^{''(2)}(\omega) \tag{3.9}$$

For isotropic and cubic systems such as those under study here, the first order susceptibility is given by equation 3.10.[6]

$$\varepsilon_{jk}^{(1)} = \begin{bmatrix} \varepsilon_{11} & 0 & 0 \\ 0 & \varepsilon_{11} & 0 \\ 0 & 0 & \varepsilon_{11} \end{bmatrix} \tag{3.10}$$

3.3 Second Order Interactions – Difference Frequency Generation

Before the advent of lasers and their associated large electric and magnetic field values, the relations described in the previous section were sufficient to describe most observed EM phenomena. Under the influence of large fields, however, all materials at some point, become non-linear, and second, third, and even higher orders of polarization are produced. Because these terms are higher order, they are, in general, of low efficiency.

relative population of the system in the state n and the total sum of $\text{Tr}\rho = 1$. Any non-zero off diagonal elements indicate that there is a coherent admixture of states n and m. The evolution of these states over time is given by the Liouville equation as 3.15.[9]

$$\frac{\partial \rho}{\partial t} = \frac{1}{i\hbar}[H, \rho]$$

(3.15)

In the case of non-linear optics, the Liouville equation becomes 3.16 which

$$\frac{\partial \rho}{\partial t} = \frac{1}{i\hbar}[H_0 + H_{int}, \rho] + \left(\frac{\partial \rho}{\partial t}\right)_{relax}$$

$$\left(\frac{\partial \rho}{\partial t}\right)_{relax} \equiv \frac{1}{i\hbar}[H_{randonm}, \rho]$$

(3.16)

includes a relaxation term due to the random fluctuations in the system due to collisions, spontaneous emissions, and similar phenomena and results in excited states returning to their ground states with a characteristic relaxation time, T_n.[10] The relaxation to the ground state is, in general, an exponential function, and equation 3.17 will be the governing relation.[11] In 3.17, $T_{nn'}$ is known as the longitudinal relaxation time. There is

$$\left(\frac{\partial \rho_{nn'}}{\partial t}\right)_{relax} = -T_{nn'} \rho_{nn'}$$

(3.17)

an additional *transverse* relaxation time which describes the relaxation between off diagonal elements.

We are now ready to determine the second order non-linear polarization term and susceptibility. A standard perturbation approach is employed, and the density operator and polarization terms are expanded as 3.18. The series expansion of ρ is then

The second order susceptibility is a third rank tensor with 3 x 3 x 3 elements. Because of crystal symmetry considerations, most of these elements are redundant, and the tensor can be represented in a reduced form. It can be shown that $\chi_{ijk}^{(2)} = \chi_{ikj}^{(2)}$. Thus, the jk elements can be represented by a single index, l. As a result, the tensor can be represented by a single 3 x 6 matrix. The valid terms for GaAs is shown as 3.22.[12]

$$\chi_{il}^{(2)} = \begin{bmatrix} 0 & 0 & 0 & \chi_{14} & 0 & 0 \\ 0 & 0 & 0 & 0 & \chi_{14} & 0 \\ 0 & 0 & 0 & 0 & 0 & \chi_{14} \end{bmatrix} \tag{3.22}$$

Also through symmetry operations, it can be shown that $\chi_{iii}^{(2)} = -\chi_{iii}^{(2)}$. The only way for this to be true is if $\chi_{iii}^{(2)} = 0$. Thus, in crystals with inversion symmetry such as silicon and germanium, all $\chi_{ijk}^{(2)}$ are equal to zero, and DFG cannot be conducted using these materials without artificially adding some asymmetry through, for example, the growth of asymmetric structures. Since GaAs and AlAs are zincblende crystals, they do not possess inversion symmetry.

We are now ready to look at the DFG process in some detail. For DFG, $\omega_2 = \omega_3 - \omega_1$. and the induced polarization in the crystal is given by 3.23. This polarization

$$P_j(\omega_2) = 2\varepsilon_0 \sum_{k,l} \chi_{jkl}(-\omega_2;\omega_3,-\omega_1)E_k(\omega_3)E_l^*(\omega_1) \tag{3.23}$$

in turn will serve to generate an EM wave at ω_2. The power developed, in general, will radiate randomly in all directions, and unless the appropriate phase matching conditions can be established, the output will be extremely weak. The equation for the output power

at ω_2 is shown as equation 3.24.[13] From 3.24 some key points need to be addressed. First, the output power is proportional to ω_2^2, so the output power will drop off rapidly as the difference between the pump beams becomes smaller and longer output wavelengths are attempted to be generated. Second, the power drops off rapidly if there are significant absorption elements in the waveguide. This became a significant driving factor in the strategy employed in this research as will be detailed in Chapter 6. Finally, the power drops off rapidly for any phase mismatch between the three wave vectors. Equation 3.25 shows the phase matching condition for DFG.[14] Since this is a subtraction process, the

$$\Delta K = k_3 - k_1 - k_2 = \frac{n(\omega_3)}{\lambda_{\omega 3}} - \frac{n(\omega_1)}{\lambda_{\omega 1}} - \frac{n(\omega_2)}{\lambda_{\omega 2}} \tag{3.25}$$

pump wave vectors are subtracted from each other vice being summed as in a sum frequency process. This makes the phase matching condition between the two processes completely different. The phase matching condition is again a major driving force in the design and growth of waveguide structures, and this topic will be addressed in great detail in Chapter 5. As will be seen in Chapter 6, the output power falls rapidly as the phase mismatch increases.

Chapter 4

Asymmetric Quantum Wells

4.1 Introduction

As shown in Chapter 1, the second order non-linear susceptibility for DFG, $\chi_{ijk}^{(2)}$, for GaAs and $Al_xGa_{(1-x)}As$ is among the highest reported for many common non-linear materials. This is true without considering any resonance terms in the equations for $\chi_{ijk}^{(2)}$, so calculated values are conservative in that the conditions are assumed to be away from any appreciable resonance effects, and the elements in the equations discussed in Chapter 3 are simplified. With the addition of quantum wells, which are easily fabricated and grown in this material system, it is possible that by tuning the quantum well band to band and inter sub-band transition energies, that resonant effects could be invoked which would greatly enhance the material values over the bulk material.

4.2 Quantum Well Band Structure

Figure 4-1 shows the basic structure of the asymmetric quantum wells under study in this research. The well consists of 60 Angstroms of GaAs followed by 40 Angstroms of $Al_{.14}Ga_{.86}As$ surrounded by $Al_{.4}Ga_{.6}As$ barriers which are 100 Angstroms thick. The allowable energy levels within the structure are determined by a self-consistent solution of the Schrödinger equation using the appropriate boundary conditions at the well boundaries. The resultant inter sub-band transition from energy level 1 to 2 within the well is shown in Figure 4-1.

Returning to the calculation of non-linear susceptibilities as discussed in Chapter 3, one can solve for the non-linear susceptibility term for a quantum well.[1] The addition of the quantum wells will disrupt the symmetry of the bulk semi-conductor as described previously. The $\chi^{(2)}$ tensor can now be shown to be of the form of equation 4.1.[2] In 4.1,

$$\chi^{(2)} = \begin{bmatrix} 0 & 0 & 0 & 0 & \chi_{15} & 0 \\ 0 & 0 & 0 & \chi_{24} & 0 & 0 \\ \chi_{31} & \chi_{32} & \chi_{33} & 0 & 0 & 0 \end{bmatrix} \qquad (4.1)$$

$\chi_{33}=\chi_{zzz}$, $\chi_{31}=\chi_{zxx}=\chi_{zyy}=\chi_{32}$, and $\chi_{15}=\chi_{xzx}=\chi_{yzy}=\chi_{24}$. Depending on the wavelength of the photon involved, χ_{33} is the dominant term in processes in which inter sub-band transitions occur while for DFG, χ_{31} is the dominate term. Unfortunately for our considerations, however, this term involves type I phase matching, whereby the pump waves are either both extraordinary or both ordinary waves.[3] In plain language, this means that both pump waves are either of the TM or TE mode type. We will show in Chapter 5 that non-linear phase matching is not possible for guided modes using these waves. Therefore, we will be using type II phase matching which involves TE-TM or TM-TE configurations. In terms of the tensor elements discussed above, this means that we will be examining the χ_{24} terms. The discussion above assumes that the quantum well was grown along the z axis. For our purposes, we shall transform the coordinates to the waveguide coordinate system since we will be assuming that the waves propagate along the z axis in Chapter 5. In our coordinate system, the quantum wells are grown in the x direction, and the waves propagate along the z axis. Using this nomenclature, and assuming an undoped well

with the valence band filled and the conduction band empty, the calculation of $\chi_{yxy}^{(2)}$ yields equation 4.2.[5] This is the term which is appropriate for the only system of waves which were found to have a solution to the phase matching condition for a guided waveguide mode as shown in Chapter 5. Some observations concerning 4.2 are in order. The resonance enhancement feature of this system is readily apparent in the last term. When the pump wave equals the interband transition energy, shown as 1.42 eV on Figure 4-1, this term is maximized due to the cancellation in the denominator. Also, since this alignment does not feature any waves perpendicular to the well, there is no enhancement term for the inter sub-band transitions as is found in the expression for $\chi_{xyy}^{(2)}$. This is unfortunate because the addition of the inter sub-band terms enhances the magnitude of $\chi_{xyy}^{(2)}$ by two additional orders of magnitude. A plot of $\chi_{yxy}^{(2)}$ as a function of pump wavelength is shown as Figure 4-2.[6] As seen in Figure 4-2, there is a strong resonance enhancement in the range of approximately 700 to 840 nm. The peak value is found to be 2.36×10^{-10} m/v at a wavelength of 835 nm. The off-resonant spectra falls rapidly to the bulk value of $\chi^{(2)}$ for DFG in this wavelength range, which is about 10^{-11} m/v. As a result, we find that the resonant enhancement feature in this region is on the order of 24 times the bulk non-resonant value. These values, however, also fall within the range of wavelengths where absorption in GaAs is significant. We will discuss this further in Chapters 6 and 7.

4.3 References

[1]   X. Qu and H. Ruda, *J. Appl. Phys.*, **75**, 54, 1994.

[2]   Y. W. Chen, *Phd Dissertation*, UCLA EE Department, 1995, p. 11.

[3]   Y. R. Shen, *The Principles of Nonlinear Optics*, John Wiley & Sons, New York,
       1984, p. 76.

[4]   E. O. Kane, *J. Phys. Chem. Solids*, **1**, 249, 1957.

[5]   Qu and Ruda (Ref 1).

[6]   Qu and Ruda (Ref 1).

what is generally considered to be normal dispersion characteristics although there are areas of slightly anomalous dispersion near the fundamental absorption edge for each
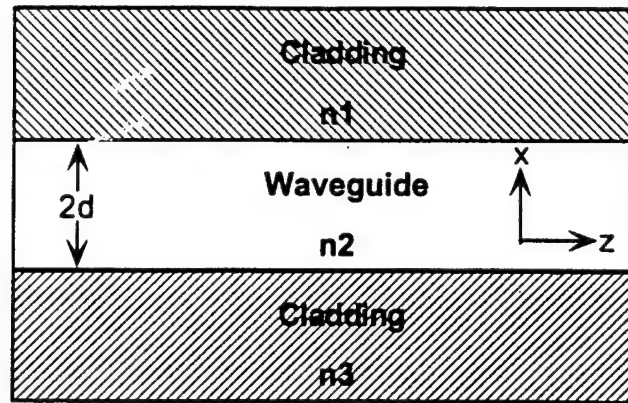

Figure 5-1. Basic Waveguide Structure

particular Al content. As expected, the anomalous region shifts upward in energy as the Al content is increased.

The next step is to solve for the propagation of each of the waves down the waveguide separately. The treatment which follows is essentially condensed from the

Table 5-1. Index of Refraction vs. Al Content and Wavelength

Wavelength	Index, $Al_{.13}Ga_{.87}As$	Index, AlAs
825 nm	3.56	2.99
895 nm	3.48	2.97
10.55 μm	3.22	2.81

work of Balanis.[3] Given that the axis of the waveguide is along the z axis, the equations which describe the electromagnetic fields are given as Equations 5.2 and 5.3. In this

$$E = E(x,y)\exp(i\,\omega t - \gamma z) \tag{5.2}$$

$$H = H(x,y)\exp(i\,\omega t - \gamma z) \tag{5.3}$$

general form, γ is the complex propagation constant given by $\alpha/2 + i\beta$. For purely propagating waves, $\alpha = 0$, and for attenuating waves, $\beta = 0$. Each solution to Maxwell's equations will depend upon the waveguide geometry and frequency of operation. The propagation constants are determined by applying the boundary conditions to the field quantities. When these fields are substituted into Maxwell's curl equations, the following relationships are obtained:

$$\frac{\partial E_z}{\partial y} + \gamma E_y = -i\omega\mu H_x \tag{5.4}$$

$$-\gamma E_x - \frac{\partial E_z}{\partial x} = -i\omega\mu H_y \tag{5.5}$$

$$\frac{\partial E_y}{\partial x} - \frac{\partial E_x}{\partial y} = -i\omega\mu H_z \tag{5.6}$$

A similar set of relationships is obtained for the magnetic field vectors. These equations can then be manipulated to elimate either E_y or H_x and the remaining component E_y or H_x can then be expressed in terms of the propagating fields E_z and H_z. Equations 5.7 and 5.8 give the results for the electric field components. In these expressions, γ and k are the

2. Substrate Mode. Waves introduced into the guide escape into the substrate. For this case, $n1 < \beta/k_0 < n3$.

3. Waveguide Mode. Waves introduced into the guide are trapped inside the waveguide and propagate down its length. For this case, $n3 < \beta/k_0 < n2$.

In the cases above, β is the magnitude of the complex longitudinal propagation constant, and k_0 is the free space propagation constant which is given by $2\pi/\lambda_0$. The relationship between these quantities is in accordance with the following. The velocity of the electromagnetic (EM) wave through any material is given by $(\epsilon\mu)^{-1/2}$, where ϵ and μ are the electric permittivity and magnetic permeability, respectively. In vacuum, ϵ_0 is equal to 8.854×10^{-12} farads/meter and μ_0 is equal $4\pi \times 10^{-7}$ henries/meter. Materials are described by relative permittivities and permeabilities which are simple numeric multipliers of the above values. For all of the dielectric materials that we shall consider here, the magnetic permeability is essentially the same as in free space, and μ shall be taken as being equal to 1. A material's relative permittivity (ϵ/ϵ_0) is also called the relative dielectric constant and is given the symbol κ.[5] In lossless, non-absorbing materials, the dielectric constant is a real number, and the index of refraction, which relates the velocity of light in a material compared to free space, will be given by the square root of the dielectric constant, $(\kappa)^{1/2}$. It can be shown mathematically that in order to trap the EM energy within the waveguide, the index of refraction in the waveguide region, n2, must be greater than the indices of refraction in both regions 1 and 3. Figure 5-3 shows a wave which is incident at an oblique angle at the waveguide -

cladding interface. In order for the wave to be completely reflected at the boundary, the angle of incidence must be greater than the so-called *critical* angle.[6] By analysis of the Fresnel reflection coefficients, it can be shown that the critical angle is given by equation 5.9, where θ_i is the angle of incidence at the boundary, and 2 and 3 refer to the waveguide

$$\theta_i \geq \theta_c = \sin^{-1}\left(\sqrt{\frac{\mu_3 \varepsilon_3}{\mu_2 \varepsilon_2}}\right) \tag{5.9}$$

$$\theta_i \geq \sin^{-1}\left(\sqrt{\frac{\varepsilon_3}{\varepsilon_2}}\right) \tag{5.10}$$

and cladding regions, respectively. As stated earlier, for the materials under study here, the relative magnetic permeabilities are equal to 1, so this equation reduces to equation 5.10. Since the sine function cannot exceed unity, one readily deduces equation 5.11, and

$$\varepsilon_3 \leq \varepsilon_2 \tag{5.11}$$

hence the index of refraction of the cladding material must be less than the index of refraction in the waveguide region for any effective waveguiding action to take place. Fortunately for our work, the AlGaAs/GaAs system provides just this sort of relationship. As given by equation 5.1 and evident in Figure 5-2, the index of refraction goes down as the Al content increases. Hence, AlAs can be used as an effective waveguide cladding. In the case of $Al_{.14}Ga_{.86}As$/AlAs system, the critical angle is equal to 58.1 degrees. To solve for the modes of propagation in the waveguide, we return once again to Maxwell's equations.

described by equation 5.17. In these expressions, h_x are the transverse propagation constants for the various regions, C_x are constants and β_z is the longitudinal propagation constant.

The odd and even modes are analyzed separately and then combined using the principle of superposition. The lowest order, TM_0 is an odd mode, and we will analyze for this mode first. There are no sources within the boundary layer, so the electric and magnetic field components must be continuous across the boundary. This gives two equations for each boundary which can then be divided to eliminate the common exponential factors. In addition, it can be shown that the propagation constants must also satisfy equations 5.18 and 5.19, so that a series of four equations and four unknowns

$$h_2^2 + \beta_z^2 = \beta_2^2 \qquad\qquad |x| \le d \qquad\qquad (5.18)$$

$$-h_{1,3}^2 + \beta_z^2 = \beta_{1,3}^2 \qquad\qquad |x| \ge d \qquad\qquad (5.19)$$

allow for the solution of the wave propagation. In equations 5.18 and 5.19, $\beta_{1,2,3}$ refer to the propagation constants in bulk material given by $\omega^2 \mu_{1,2,3}\varepsilon_{1,2,3}$. By using equation 5.18 and 5.19, and then dividing the equations which result after applying the boundary conditions, equation 5.20 is obtained. The next step is to solve for the modes which can

$$\frac{\varepsilon_{1,3}}{\varepsilon_2}(h_2 d)\tan(h_2 d) = h_{1,3}d \qquad\qquad (5.20)$$

be supported by the particular waveguide. For simplicity, we shall assume that regions 1 and 3 are of the same material, so that $h_1=h_3$, and $\varepsilon_1=\varepsilon_3$. In order for the waveguide to act
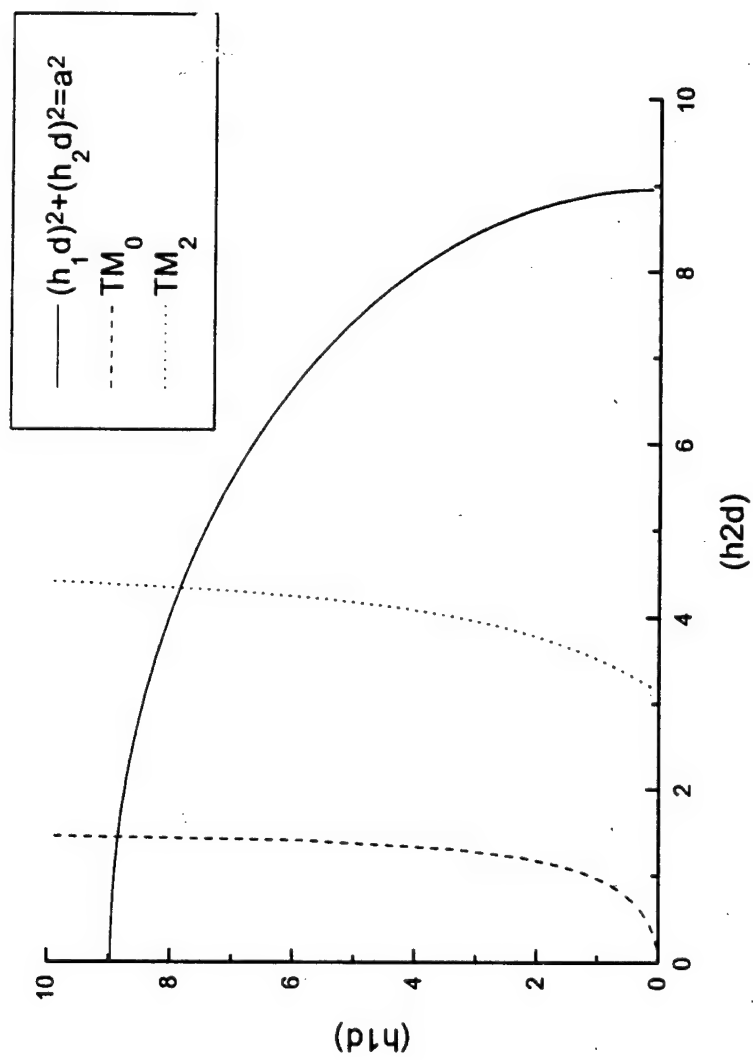
Figure 5-4. Graphical Solution of Propagation Constants for Dielectric Waveguide
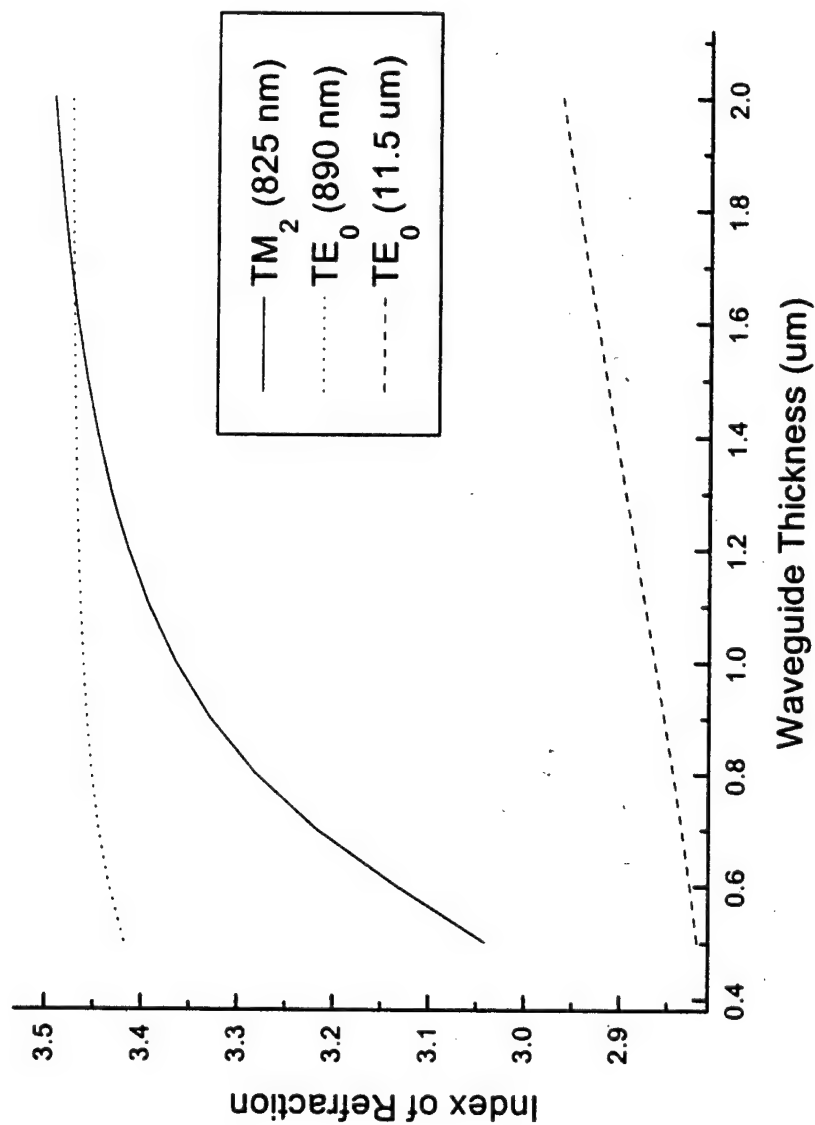
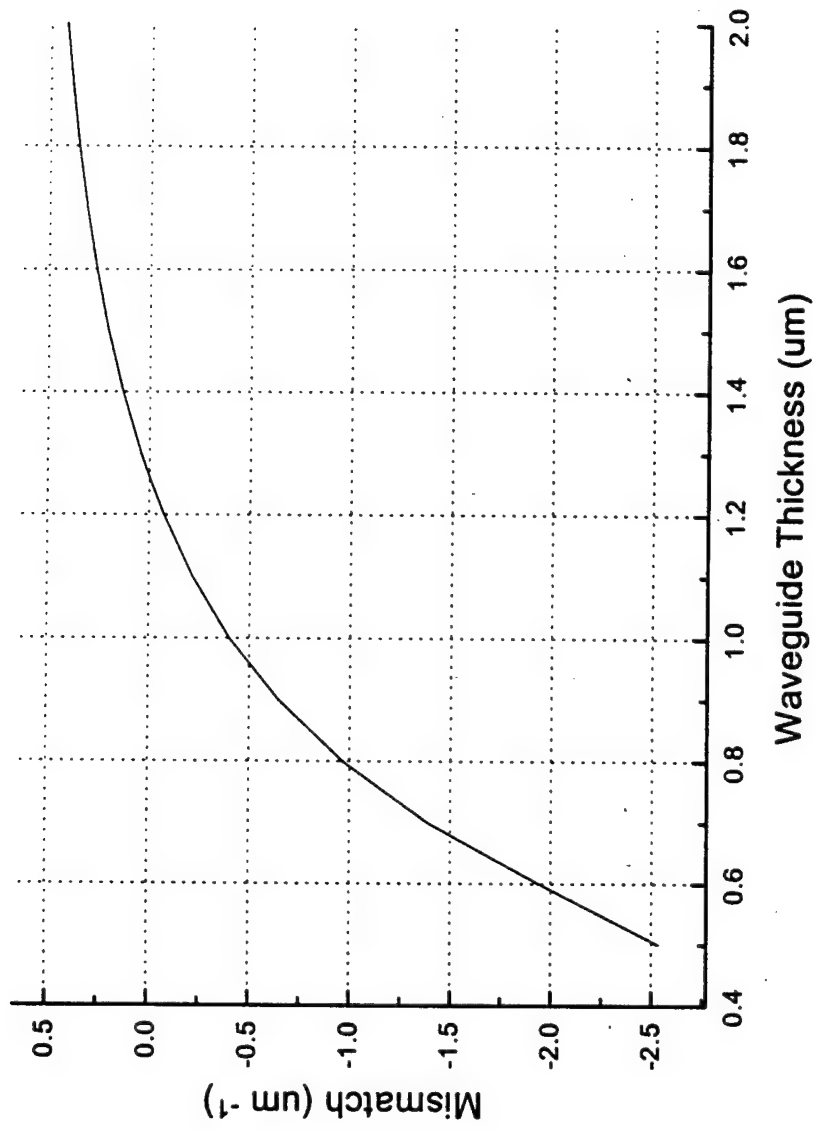**Figure 5-5. Effective Index of Refraction vs. Waveguide Thickness**
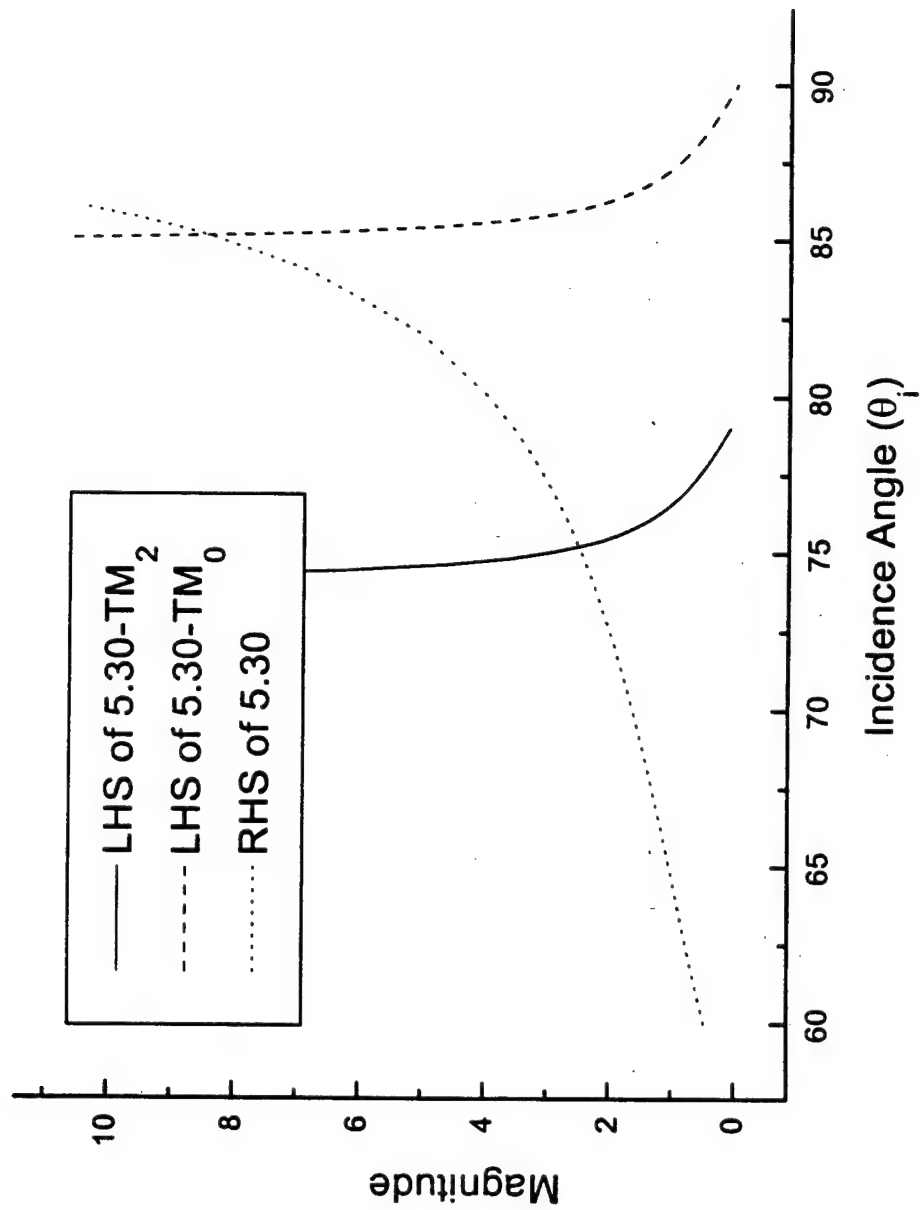
57

Figure 5-6. Mismatch vs. Waveguide Thickness

Figure 5-7. Raytrace Solution of Waveguide Propagation

Legend:
—— LHS of 5.30-TM_2
---- LHS of 5.30-TM_0
······ RHS of 5.30

X-axis: Incidence Angle (θ_i)
Y-axis: Magnitude

Hence, since waves of different frequencies travel at different velocities the waves would propagate away from each other and power generation would be poor without some kind of restraint. By forcing the waves to travel down the waveguide with different incident angles at the interface boundaries, the propagation velocity along the waveguide axis can effectively be "tuned" to keep the waves in synch.

We now return to our transfer matrix description of the quantum well structure. The objective is to determine the effective propagation constant across the entire stack so that the previous analysis concerning the reduction in the index of refraction and phase matching can be repeated using this value. We shall restrict our discussion initially to the 890 nm TE_0 mode wave. Figure 5-8 shows a wave incident on a stratified layer such as a stack of quantum wells and barriers. We immediately run into a problem when analyzing
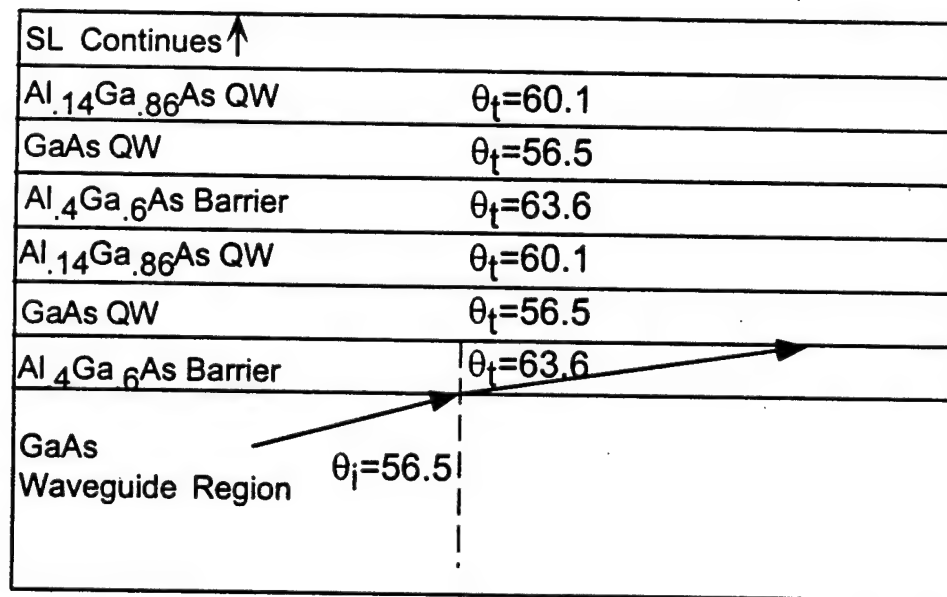
SL Continues ↑	
$Al_{.14}Ga_{.86}As$ QW	$\theta_t=60.1$
GaAs QW	$\theta_t=56.5$
$Al_{.4}Ga_{.6}As$ Barrier	$\theta_t=63.6$
$Al_{.14}Ga_{.86}As$ QW	$\theta_t=60.1$
GaAs QW	$\theta_t=56.5$
$Al_{.4}Ga_{.6}As$ Barrier	$\theta_t=63.6$
GaAs Waveguide Region	$\theta_i=56.5$

Figure 5-8. Wave Propagation Through QW Structure

Equation 5.33

$$M(d) = \begin{bmatrix} \cos\beta_1 & -\dfrac{i}{p_1}\sin\beta_1 \\[2ex] -ip_1\sin\beta_1 & \cos\beta_1 \end{bmatrix} \begin{bmatrix} \cos\beta_2 & -\dfrac{i}{p_2}\sin\beta_2 \\[2ex] -ip_2\sin\beta_2 & \cos\beta_2 \end{bmatrix} \begin{bmatrix} \cos\beta_3 & -\dfrac{i}{p_3}\sin\beta_3 \\[2ex] -ip_3\sin\beta_3 & \cos\beta_3 \end{bmatrix}$$

Equation 5.34

$$M(1,1) = \cos\beta_1\cos\beta_2\cos\beta_3 - \frac{p_2}{p_1}\sin\beta_1\sin\beta_2\cos\beta_3 - \frac{p_3}{p_1}\sin\beta_1\cos\beta_2\sin\beta_3 - \frac{p_3}{p_2}\cos\beta_1\sin\beta_2\sin\beta_3$$

$$M(1,2) = -\frac{i}{p_1}\sin\beta_1\cos\beta_2\cos\beta_3 + \frac{ip_2}{p_1 p_3}\sin\beta_1\sin\beta_2\sin\beta_3 - \frac{i}{p_2}\cos\beta_1\sin\beta_2\cos\beta_3 - \frac{i}{p_3}\cos\beta_1\cos\beta_2\sin\beta_3$$

$$M(2,1) = -ip_1\sin\beta_1\cos\beta_2\cos\beta_3 - ip_2\cos\beta_1\sin\beta_2\cos\beta_3 - ip_3\cos\beta_1\cos\beta_2\sin\beta_3 + \frac{ip_3 p_1}{p_2}\sin\beta_1\sin\beta_2\sin\beta_3$$

$$M(2,2) = \cos\beta_1\cos\beta_2\cos\beta_3 - \frac{p_1}{p_2}\sin\beta_1\cos\beta_2\sin\beta_3 - \frac{p_1}{p_3}\sin\beta_1\sin\beta_2\cos\beta_3 - \frac{p_2}{p_3}\cos\beta_1\sin\beta_2\sin\beta_3$$

represented the waveguide half-width. In this case we are summing over the entire thickness of the waveguide. We perform the analysis for two waves which are 10 nm apart in wavelength. This will be the case as described in the split Ti:sapphire
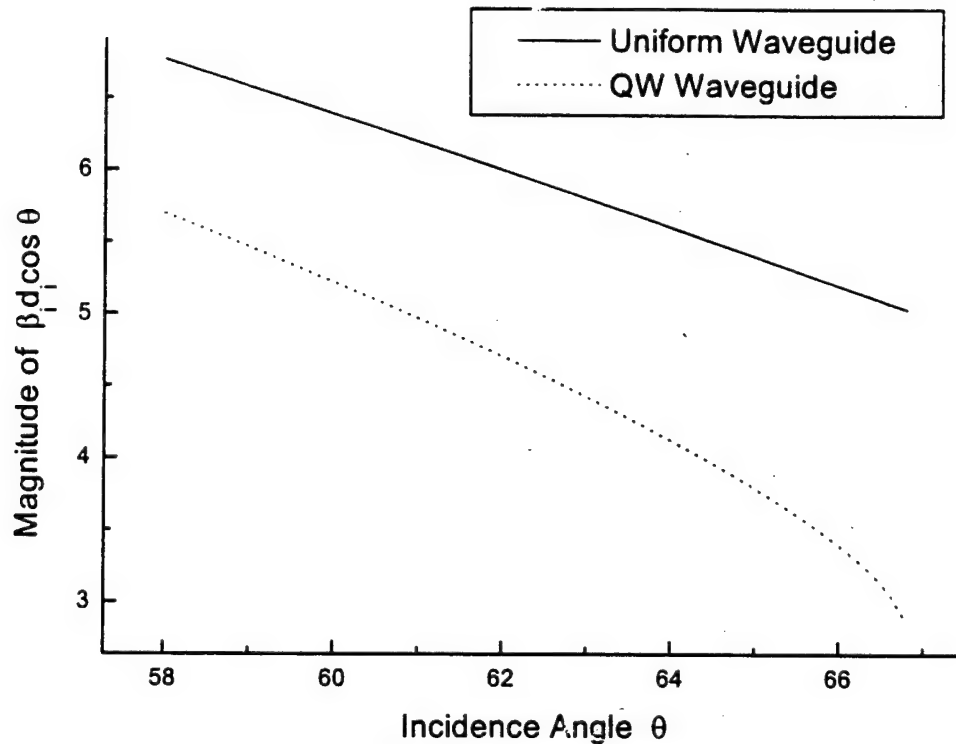

Figure 5-9. Magnitude of $\beta_i d_i \cos\theta_i$ vs. Angle of Incidence

experiment described in Chapter 8. The two waves will be 890 and 900 nm, which describes the splitting of the mode locked laser centered at 895 nm. We will assume that the only significant phase changes occur at the reflective interfaces, and that the transmitted waves will not suffer significant phase changes as they transit the thin quantum well layers. So, the solution will be essentially solving 5.30 once again, except

containment. Thus the range of allowable propagation angles is somewhat limited. The calculation procedure is fairly straightforward since each layer which is composed of the same material will have the same propagation angle, so only three angles need to be calculated. When solving these equations, it is important to determine which mode of propagation is determined by the solutions of the modified 5.30. The tangent function could possibly have several intercepts with the rhs of 5.30 within the range of interest due to the large value of the bulk propagation constant which makes the value of $\beta_i d_i$ a moderately large number. Being inside the argument of the tangent function, this gives the function several zeros in the range of 50 to 90 degrees. Since the tangent function is unchanged by a translation of π radians, it can be difficult to determine which mode an intercept point represents. In order to determine the mode, one looks at the argument of the tangent function and locates the poles and zeros. Equations 5.38 shows the tangent function arguments for the first three TE modes. For the zero order mode, the zero will

$$\tan(\frac{VPL}{2}) = \frac{\sqrt{\frac{\varepsilon_2}{\varepsilon_1}\sin^2\theta_i - 1}}{\sqrt{\frac{\varepsilon_2}{\varepsilon_1}}\cos\theta_i} \qquad \text{Zero Order}$$

$$\tan(\frac{VPL - \pi}{2}) = \frac{\sqrt{\frac{\varepsilon_2}{\varepsilon_1}\sin^2\theta_i - 1}}{\sqrt{\frac{\varepsilon_2}{\varepsilon_1}}\cos\theta_i} \qquad \text{First Order} \qquad (5.38)$$

$$\tan(\frac{VPL - 2\pi}{2}) = \frac{\sqrt{\frac{\varepsilon_2}{\varepsilon_1}\sin^2\theta_i - 1}}{\sqrt{\frac{\varepsilon_2}{\varepsilon_1}}\cos\theta_i} \qquad \text{Second Order}$$

quantum wells in the given sample, or (2) the minimum VPL required for the mode number. It was found that the quantum well limit applied for the 0 order modes, while the VPL requirement applied for the higher order modes. The thickness was then varied until the upper limit was reached. The upper limit was determined by the maximum incidence angle allowed at the $GaAs/Al_4Ga_6As$ waveguide-barrier interface as discussed earlier. This angle is 66.8 degrees. Figures 5-10, 5-11, and 5-12 detail the results from the $TM_0 - TE_0$, $TM_1 - TE_1$, and $TM_2 - TE_2$ combinations, respectively. It was found that the restrictions discussed earlier make the phase matching problem much more difficult in the multi-layered case. The figures clearly show that the only system which has a phase matched solution is the $TM_0 - TE_0$ system, and this solution occurs for a waveguide thickness in the vicinity of .18 to .20 μm depending on the number of quantum wells added to the structure. The phase matched point moves slightly to the right as the number of quantum wells is increased. If more than 8 quantum wells are placed in the structure, however, the minimum channel thickness becomes too great to achieve phase matching due to the inherent thickness of the quantum wells themselves. In addition, unlike the uniform waveguide case discussed previously, there is little or no overlap region between higher order modes and lower order modes where greater differences in propagation constants can be expected and phase matching more tunable. In this system, the only structures which will support simultaneous propagation of different order modes are the one with thickness values at the extreme edge of allowable values, and in these borderline cases, the phase mismatch is excessive and not usable for DFG. Herein lies the great difficulty in observing the DFG signal from the quantum well
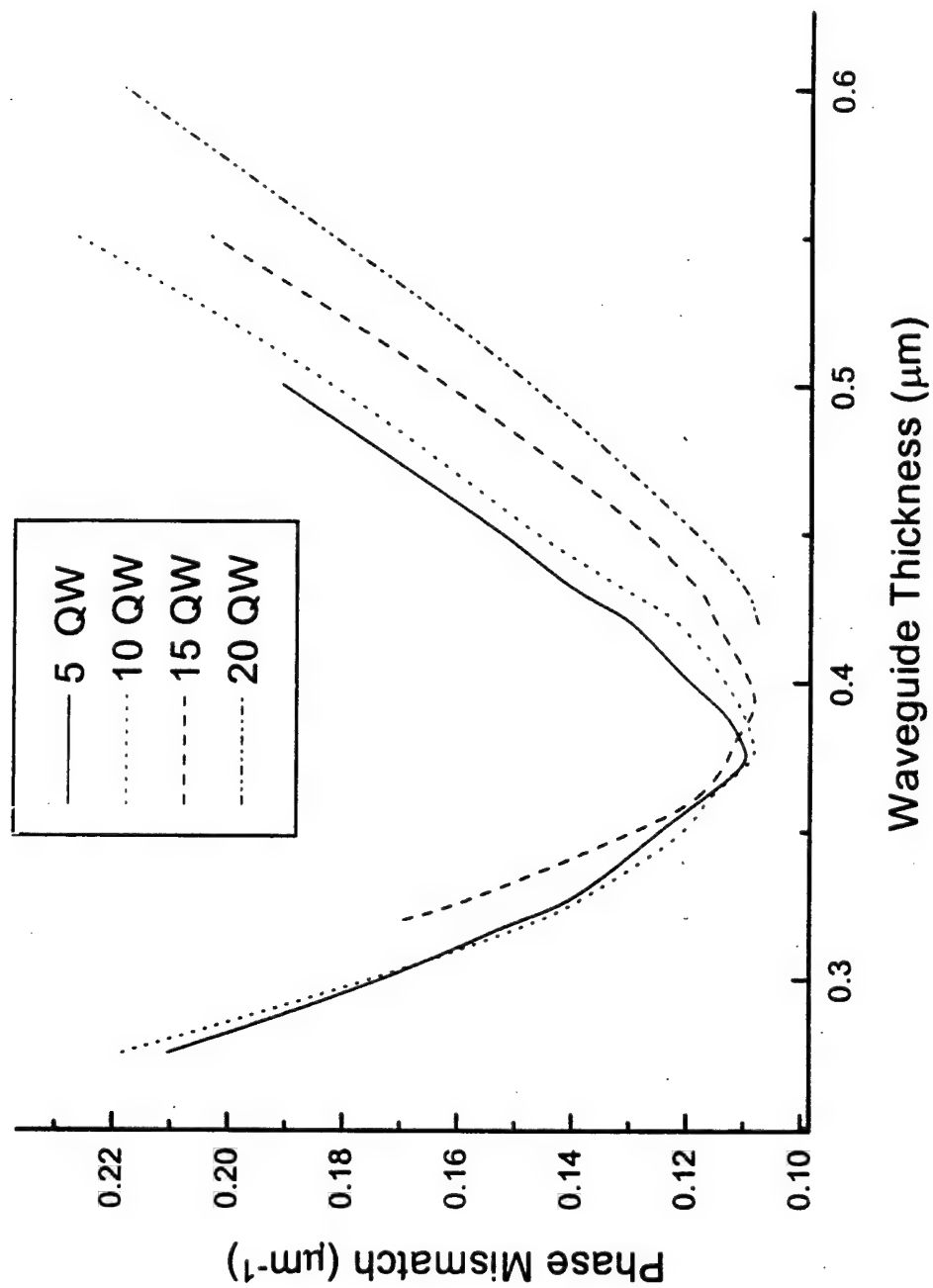
Figure 5-11. Phase Matching for TM$_1$ – TE$_1$ Wave System

Legend:
- 5 QW
- 10 QW
- 15 QW
- 20 QW

X-axis: Waveguide Thickness (μm)

Y-axis: Phase Mismatch (μm^{-1})

waveguide system. The only structures which have solutions are prohibitively thin, on the order of 2000 Angstroms, and coupling into the waveguide is difficult at best. In addition, with this thin waveguide structures, the uniformity and accuracy requirements become more stringent, and there is less slack allowed for material imperfections, growth non-uniformities, and impurities. It should be noted that the systems of waves shown in Figures 5-10 through 5-12 represent the best phase matching possible in each case.

This is not to say that waves outside of these boundaries will not travel down the general vicinity of the waveguide and quantum well structure. These are solutions for *guided* modes within the waveguide. There are the so-called *leaky* waves which will propagate some distance down the waveguide, but undergo radiative losses to both the substrate and cap layers, and thus the efficiency in both power generation and transmission are greatly reduced.[12] This is a sort of brute force method whereby if one pumps enough energy into the channel, then the desire results may still be seen, but the power generated will be extremely low.

5.3. Waveguide Coupling

To complete the discussion of waveguides, it is necessary to spend a little time discussing the method of coupling the pump waves into the waveguide. Clearly the power generated through DFG will be directly related to the amount of pump energy which can be introduced into the channel. For our research, the pump beams were incident on the side face of the structure as described elsewhere. This method is rather inefficient and difficult to align with the very narrow waveguide region. Figure 5-13

illustrates the geometry required for a particular wave propagation. For our research, the samples were polished 60 degrees on the edge to produce an external angle of incidence of approximately 30 degrees, and then the sample was adjusted to provide the proper incidence angle for the particular guided mode under study. Equation 5.39 shows the

$$\theta_i = \theta_r = \left(\theta_{polish} + \theta_t\right) = \left(90 - \theta_{i-ext} + \theta_t\right) \qquad (5.39)$$

geometrical relationship between the external angle of incidence and the incidence angle at the waveguide – cladding interface which is the critical value for guided mode operation. The angles indicated in 5.39 are displayed in Figure 5-13. The waveguide transmission angle can be removed via Snell's Law, and equation 5.40 results. This gives the internal angle of incidence vs. the external angle of incidence, θ_{i-ext}.

$$\theta_i = 90 - \theta_{i-ext} + \sin^{-1}\left(\frac{\sin(\theta_{i-ext})}{\sqrt{\varepsilon_{guide}}}\right) \qquad (5.40)$$

The power coupling efficiency of this method is rather poor. Due to the large difference between the index of refraction of the dielectric material and the air, much of the incident energy is reflected. Equations 5.41 and 5.42 give the *Reflectivity* values for the TM and TE waves respectively.[13] Using an external incidence angle of 30 degrees,

$$R_{TM} = \frac{\tan^2(\theta_{i-ext} - \theta_t)}{\tan^2(\theta_{i-ext} + \theta_t)} \qquad (5.41)$$

$$R_{TE} = \frac{\sin^2(\theta_{i-ext} - \theta_t)}{\sin^2(\theta_{i-ext} + \theta_t)} \qquad (5.42)$$

on GaAs, it is seen that this value is .27 and .37 for 890 nm TM and 900 nm TE waves

5.4 References.

[1.]   Y. Kokubo and I. Ohta, *J. Appl. Phys.*, **81**, 2042, 1997.

[2]   E. Palik, *Handbook of Optical Constants of Solids II*, Academic Press, Boston, 1991, p. 513.

[3]   Constantine A. Balanis, *Advanced Engineering Electromagnetics*, John Wiley & Sons, New York, 1989, chapter 8.

[4]   Balanis (Ref 3), p. 431-432.

[5]   Henry Kressel and J. K. Butler, *Semiconductor Lasers and Heterojunction LEDs*, Academic Press, New York, 1977, p. 120.

[6]   Balanis (Ref 3), p. 196.

[7]   Balanis (Ref 3), p. 256.

[8]   David E. Thompson and Paul D. Coleman, *IEEE Transactions on Microwave Theory and Techniques*, **MTT-22**, 995, 1974.

[9]   Max Born and Emil Wolf, *Principles of Optics*, Pergamon Press, New York, 1987, p. 55.

[10]   Balanis (Ref 3), p. 437.

[11]   Born (Ref 9), p. 67.

[12]   Dietrich Marcuse, *Theory of Dielectric Optical Waveguides*, Academic Press, New York, 1991.

[13]   Born (Ref 9), p. 42.

[14]   Palik (Ref 2), p. 760.
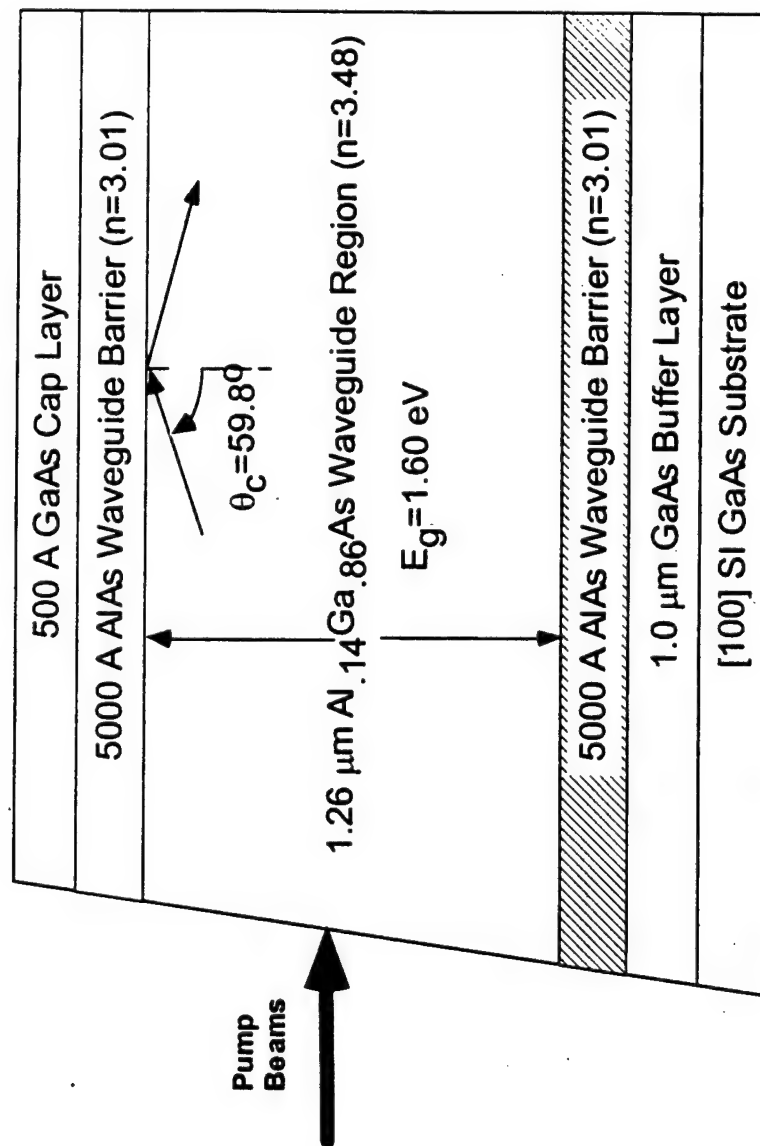
Figure 6-1. Uniform Waveguide for DFG of 11.5 μm Waves
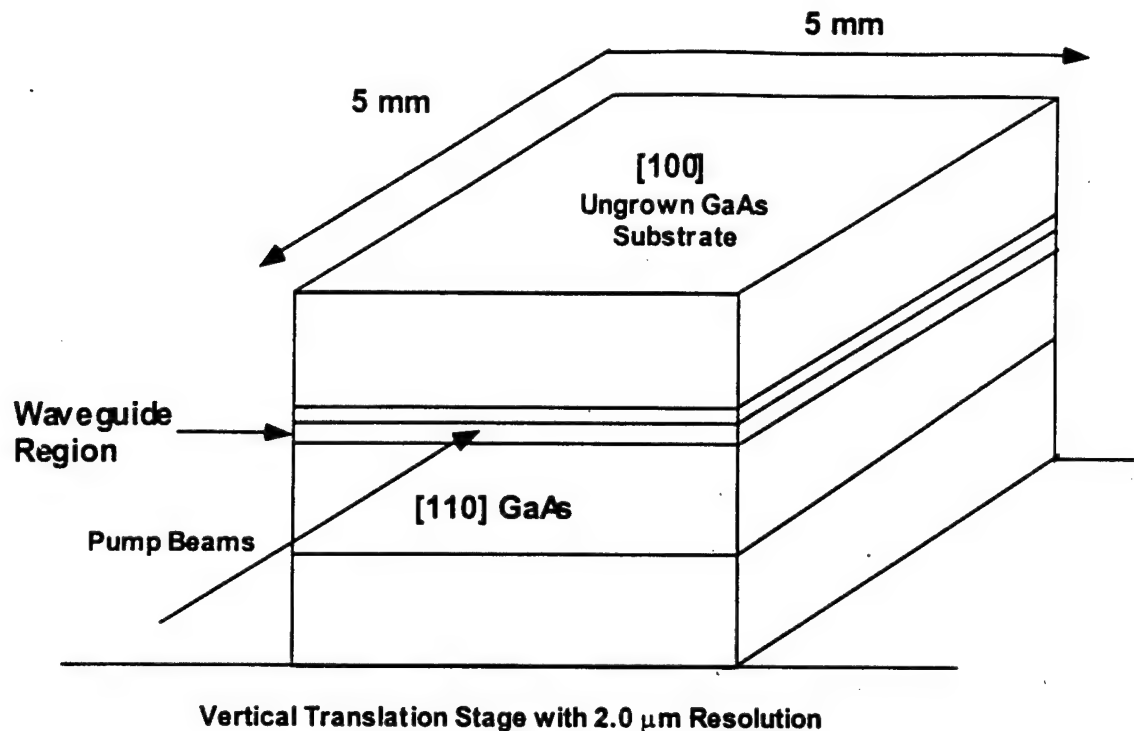
The figure shows a layered waveguide structure with the following layers (top to bottom):

- 500 A GaAs Cap Layer
- 5000 A AlAs Waveguide Barrier (n=3.01)
- 1.26 μm Al$_{.14}$Ga$_{.86}$As Waveguide Region (n=3.48), θ_c=59.8°, E_g=1.60 eV
- 5000 A AlAs Waveguide Barrier (n=3.01)
- 1.0 μm GaAs Buffer Layer
- [100] SI GaAs Substrate

Pump Beams

81

5 mm

5 mm

[100]
Ungrown GaAs
Substrate

Waveguide Region

[110] GaAs

Pump Beams

Vertical Translation Stage with 2.0 μm Resolution

Figure 6-2. Sample "Sandwich" for DFG Measurements

region is extremely thin and close to the top of the sample, a method was desired to prevent the input light beams from diffracting over the top edge of the sample and providing a false indication of output during the alignment procedure. In addition, it was desired that a larger range of motion could be established on the vertical translation stage when aligning the beams with the waveguide without having the beams go above the sample and directly strike the detector. Hence the sandwich structure of Figure 6-2 was devised. Following the preparations listed above, pieces of ungrown GaAs substrate with polished faces were attached with epoxy to the upper and lower faces of the sample, forming a stack approximately 1 mm tall. The sample was then mounted on a vertical

translation stage which had 2.0 μm resolution in movement. The sample could then be translated up and down as desired for proper input beam placement.

The experiment setup including lasers and all assorted equipment is shown as Figure 6-3. The output of the two lasers was combined in a conventional beam splitter. The output from the Ti:sapphire laser was passed through a ½ wave plate in order to control the orientation of the polarization of this wave. The output of the laser diode was passed through a mechanical chopper which was coupled to a lock-in amplifier to provide a greater signal to noise ratio. The combined output of both lasers was passed through a focusing lens with a focal length of 11 mm and a spot size of 1.3 μm. The rather long focal length ensured that the divergence of the waves was not too severe upon entering the structure, since there is no horizontal containment on the setup. The HgCdTe detector is a general purpose IR detector with good responsivity in the range of 5 to 12 μm. It was cooled to 77 K using LN_2 during measurements in order to reduce the background thermal noise signature. The pump signals were removed at the output by a long pass filter which passed signals with wavelengths greater than 9 μm. The output of the detector was applied to a lock-in amplifier.

The first step in setting up a measurement on a new sample was to align the waveguide with the pump beams. As discussed earlier, the waves need to strike the surface of the waveguide at the proper angle and the proper position in order to traverse the waveguide efficiently. The output of the laser diode was used for this purpose. Since the output energy of this diode was above the bandgap energy of GaAs, its signal was absorbed by all of the regions in the sandwich stack with the exception of the waveguide
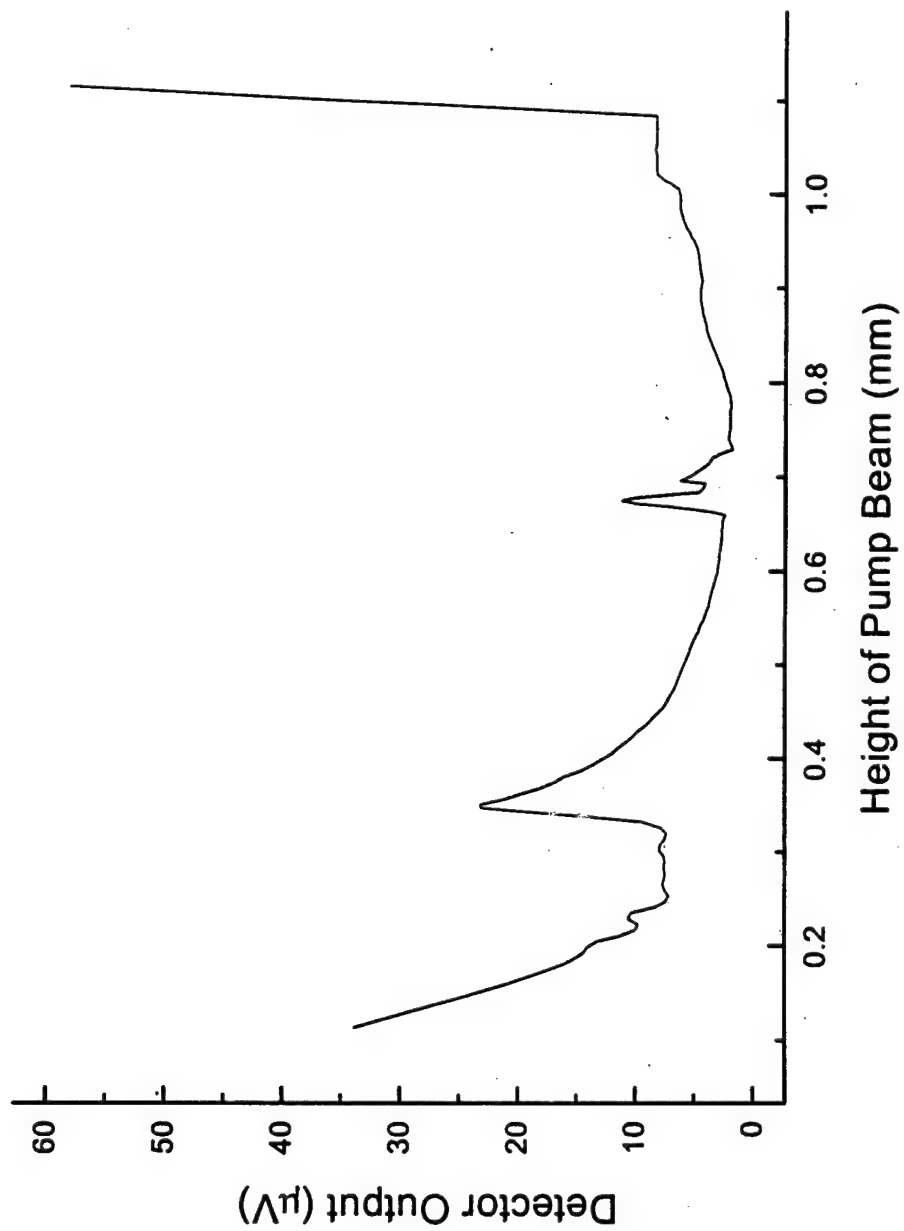
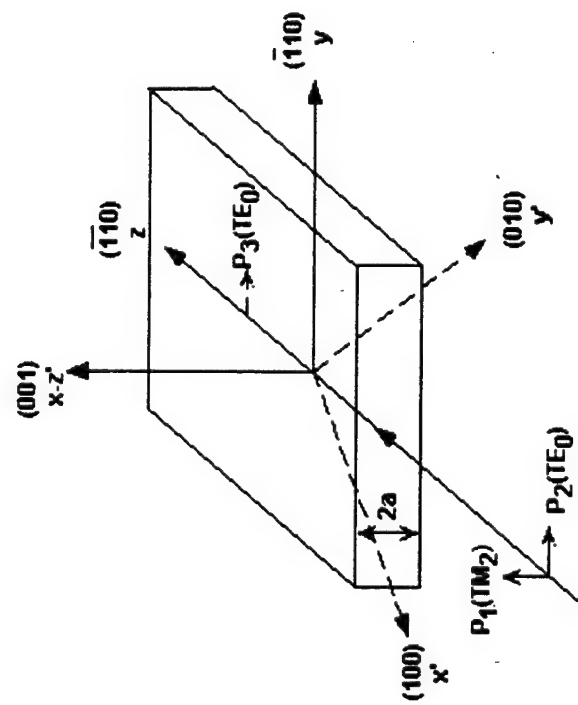Figure 6-4. Alignment of Pump Beams with Waveguide Region
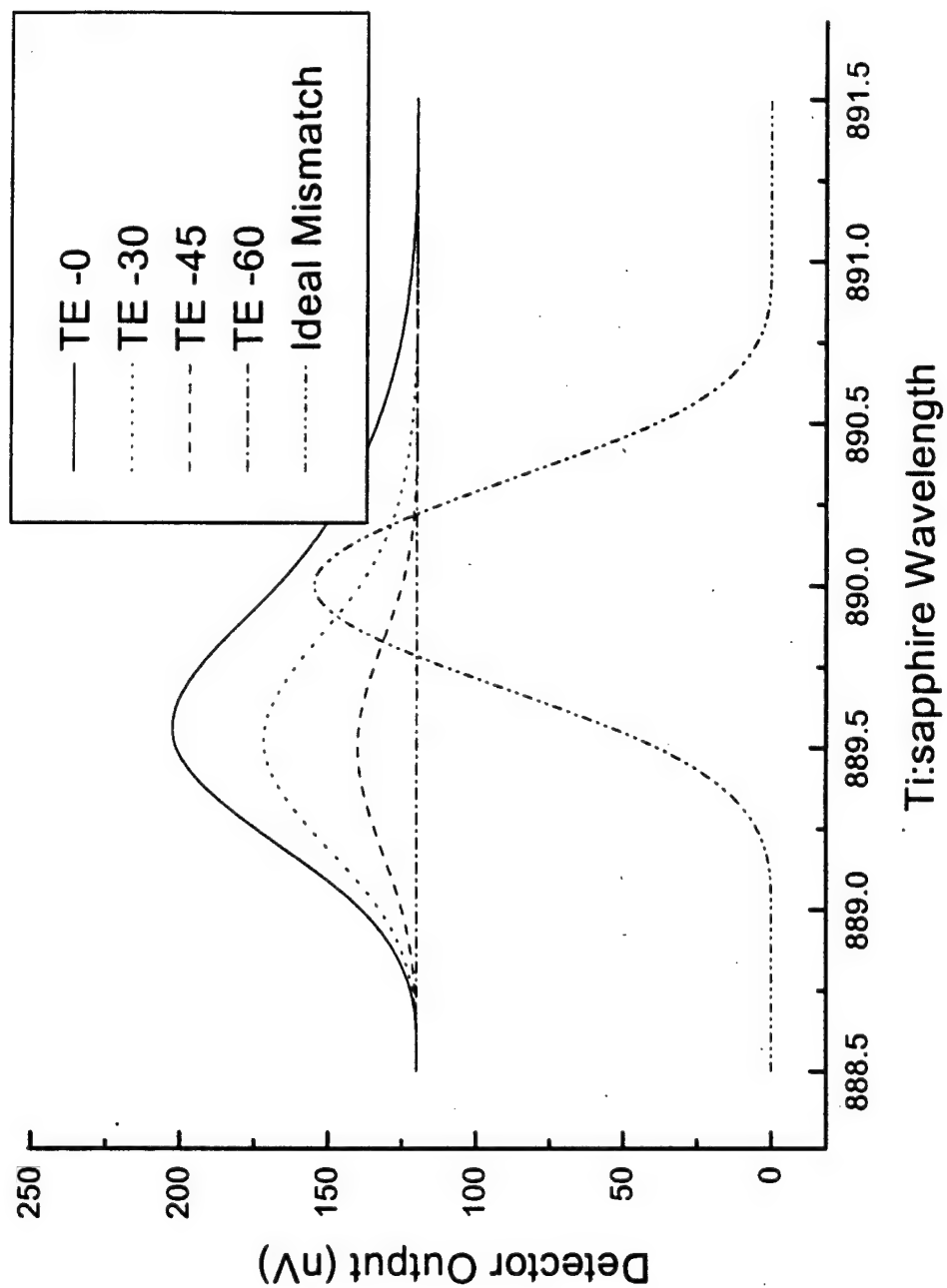
Figure 6-5. Waveguide and Crystal Coordinate System

Figure 6-6. DFG Output signal vs. TE₀ Pump Wavelength

6.4 References

[1]   David E. Thompson and Paul D. Coleman, *IEEE Transactions on Microwave*

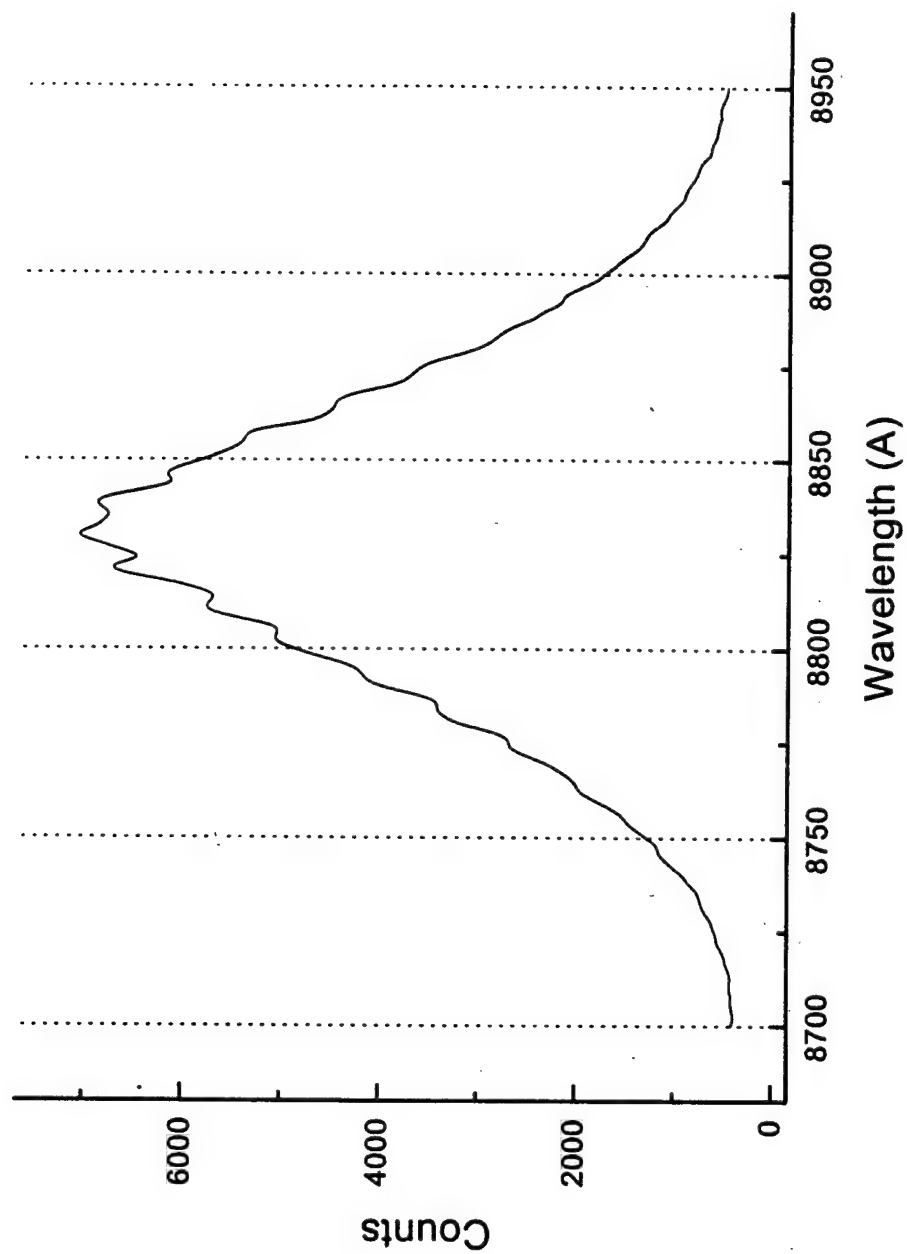*Theory and Techniques,* **MTT-22**, 995, 1974.

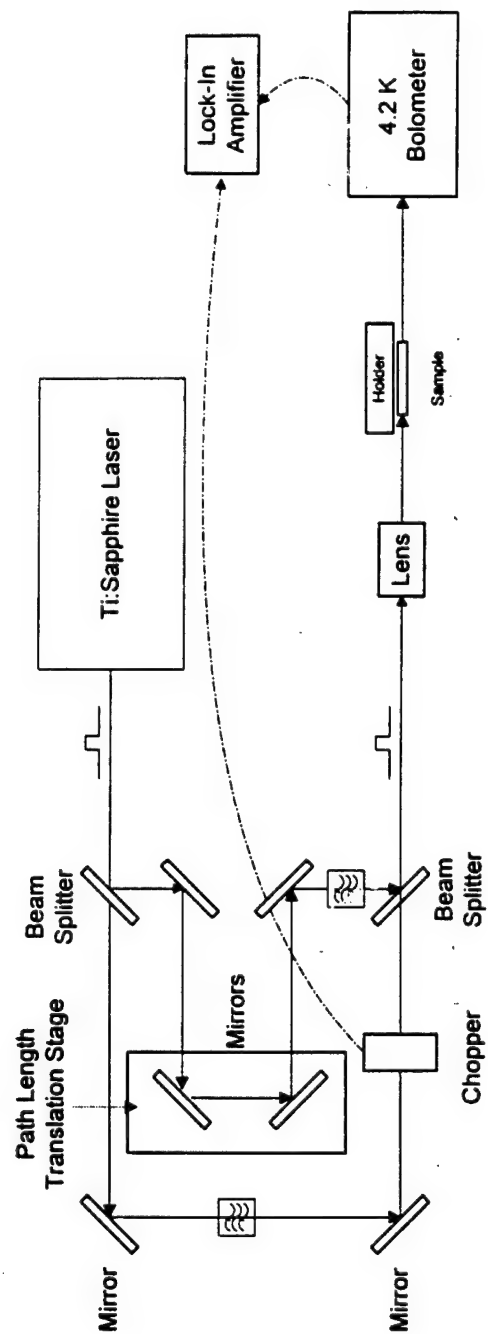Figure 7-1. Spectrum of Mode-locked Ti:sapphire Laser

95

Figure 7-2. Experimental Setup for Split Laser Approach

single mirror, we were able to translate the functions of the auto-correlator into a dual pulse overlap correlator in a fairly rapid fashion. In this manner, by observing the output signal from our modified correlator, we were able to adjust the path length to achieve path length equality and path synchronization.

7.3 Results

As discussed in Chapter 6, we did not observe any higher order modes in our waveguide structures, beyond those which were present at the input. As a result, we were limited to the $TM_0 - TE_0$ or $TE_0 - TM_0$ type interactions. Of all the possible wave interactions, these groups provided solutions with the largest waveguide thickness. Solving the equations discussed in Chapter 5, it is found that for the $TM_0 - TE_0$ system, the required waveguide thickness is .16 μm for a uniform GaAs waveguide. This is an extremely thin waveguide, and poses a very difficult wave coupling challenge. In addition, even with the input spot size minimized to 1 μm in diameter, the efficiency of energy coupled into the waveguide system is fairly poor. For instance, the area of the 1.0 μm beam is determined to be 0.79 $μm^2$, while the area of the illuminated waveguide region is .16 $μm^2$. This represents another 80 percent loss factor added to our calculations, and maybe too severe to overcome.

This value can be increased somewhat by utilizing the AQW structure as discussed in Chapter 5. The thickness required for a waveguide with 8 AQW's is .2 μm. Sample structures were grown and tested in the sample configuration as shown in Figure 7-3. We found that it was very difficult to differentiate the waveguide region from the

surrounding material. Unlike the previous case where we had a fairly thick waveguide and the ability to probe it with a 826 nm wave, we have a very thin waveguide and no energy differentiation between the material in the waveguide and the material in the substrate. We attempted to "visually" align the signals with the waveguide, which should have been feasible given the large size of the beam compared to the waveguide region, we did not observe the peaking of the transmitted signal with change in incident angle as we did in Chapter 6.

We also determined that our choice of detector in this case (although driven by those available at the time), was not an optimum one. The bolometer provides an output signal based upon the change in resistance of the detector due to the incidence of external EM signals. The detector is mounted on a heat sink which quickly returns it to its steady state temperature following its heat-up, and it returns to this equilibrium value in an exponential manner with a time constant τ_r. In addition, it heats up or responds to incident radiation with another time constant τ_i. The output response vs. chopping frequency is shown as Figure 7-2.[2] From the slope of the curve, we determine that the bolometer response time constant is on the order of 2 ms, which makes detection of our pulse train very inefficient, on the order of .00006 percent. Thus, a different detector will have to be procured in order to conduct this research.

7.4 References

[1]   Coherent Laser Group, *Operator's Manual, Mira Model 900 Laser,* Coherent,
        Inc., 1991, p. 7-21.

[2]   Infrared Laboratories, Inc., *HDL-5 Instruction Manual*, Infrared Laboratories,
        1997.

out to be the most important element in analyzing the reasons behind why certain samples produced results while others did not. It is very difficult to determine the "whys" behind a particular result, if a clear picture of the "whats" is not present. Thus, we devoted a large portion of our research to establishing control over our sample growths.

Next, we investigated the addition of AQWs to our waveguide structure. We found that the addition of multi-layers to our device complicated the phase matching requirements and greatly restricted the acceptance angles which would produce the desired results. As a result, the multi-mode solutions disappeared and greatly reduced the utility of the waveguide in providing a phase matching medium. In addition, we effectively lost the ability to use the $Al_xGa_{(1-x)}As$ as the waveguiding material. With our MBE system, we can grow $Al_xGa_{(1-x)}As$ layers with two different values of x, along with AlAs, giving us three possible $Al_xGa_{(1-x)}As$ type layers. If $Al_xGa_{(1-x)}As$ instead of GaAs is used as the material for the low quantum well, then an $Al_yGa_{(1-y)}As$ layer will be required for the high quantum well, and AlAs is the only remaining possibility for the barrier material. Since the waveguide itself is constructed of AlAs, this would preclude any waves from entering the AQW region since if the wave has an angle of incidence greater than the critical angle at the waveguide-cladding interface, then it will also be greater than the critical angle at the waveguide-barrier interface, and no energy will enter the wells.

$Al_xGa_{(1-x)}As$ system could be more thoroughly evaluated with high power monochramatic CW signals. In this manner, the range of output signals would be limited only by the detectors, and the resonance enhancement of the AQWs could be fully explored.

In the meantime, the efficiency of DFG in the uniform waveguide can be pursued and perfected, including the study of DFG efficiency vs. Al content and implementation of anti-reflective coatings to increase the coupling efficiency. In addition, a number of better laser diodes have been introduced in the last two years, and a high power laser diode should be procured at 890 nm in wavelength. The Ti:sapphire can easily be tuned to 826 nm and beyond, so in this way, a broader spectrum of DFG could be pursued for relatively little increased cost. In addition, the ability of having both of the pump wavelengths below the bandgap energy level would allow the continued investigation of the AQW structure since the low quantum well could be made of GaAs.

Finally, since the split Ti:sapphire approach produces pulsed signals which have duty cycles below the bolometer's detection threshold, a far IR photo-detector should be obtained. Again, many advances have been made in the field of detectors over the past several years, and detectors out to nearly 100 μm are now commercially available and could be used to continue this line of research.